

# 1 Remote sensing and modeling analysis of the extreme dust storm hitting 2 Middle East and Eastern Mediterranean in September 2015

3  
4  
5 Solomos Stavros<sup>1</sup>, Albert Ansmann<sup>2</sup>, Rodanthi-Elisavet Mamouri<sup>3</sup>, Ioannis Binietoglou<sup>1,5</sup>, Platon  
6 Patlakas<sup>4</sup>, Eleni Marinou<sup>1,6</sup> and Vassilis Amiridis<sup>1</sup>

7  
8 <sup>1</sup>Institute for Astronomy, Astrophysics, Space Applications and Remote Sensing (IAASARS), National  
9 Observatory of Athens, Athens, Greece

10 <sup>2</sup>Leibniz Institute for Tropospheric Research, Leipzig, Germany

11 <sup>3</sup>Cyprus University of Technology, Department of Civil Engineering and Geomatics, Limassol, Cyprus

12 <sup>4</sup>School of Physics, Division of Environment and Meteorology, University of Athens, Athens, Greece

13 <sup>5</sup>National Institute of R&D for Optoelectronics, Magurele, Ilfov, Romania

14 <sup>6</sup>Laboratory of Atmospheric Physics, Physics Department, Aristotle University of Thessaloniki, 54124,  
15 Thessaloniki, Greece

16  
17 **Abstract** The extreme dust storm that affected Middle East and the Eastern Mediterranean in  
18 September 2015 resulted in record-breaking dust loads over Cyprus with aerosol optical depth  
19 exceeding 5.0 at 550 nm. We analyze this event using profiles from the European Aerosol Research  
20 Lidar Network (EARLINET) and the Cloud-Aerosol Lidar and Infrared Pathfinder Satellite Observation  
21 (CALIPSO) as well as geostationary observations from the Meteosat Second Generation - Spinning  
22 Enhanced Visible and Infrared Imager (MSG-SEVIRI) and high resolution simulations with the  
23 Regional Atmospheric Modeling System (RAMS). The analysis of modeling and remote sensing data  
24 reveals the main mechanisms that resulted in the generation and persistence of the dust cloud over  
25 Middle-East and Cyprus. A combination of meteorological and surface processes is found: (a) the  
26 development of a thermal low at the area of Syria that results in unstable atmospheric conditions  
27 and dust mobilization at this area; (b) the convective activity over Northern Iraq that triggers the  
28 formation of westward moving haboobs that merge with the previously elevated dust layer; and (c)  
29 the changes in land use due to war at the areas of Northern Iraq and Syria that enhances dust  
30 erodibility.

## 32 **1. Introduction**

33

34 A record dust storm affected the entire Middle East and Cyprus in September 2015. Remote sensing  
35 and in-situ measurements of Arabian dust from this episode during 7-11 September 2015 are  
36 presented by Mamouri et al. (2016) for the station of Limassol (34.7°N, 33°E). As reported in this  
37 article, the extreme amounts of dust over Middle East and the Eastern Mediterranean originate  
38 from the desert and arid areas of Syria and Northern Iraq. Triggered by this work, we analyze here  
39 the main processes that resulted in the mobilization of dust due to a combination of cyclonic flow  
40 and haboob formation.

41 Haboobs are local and mesoscale atmospheric density currents that mobilize huge amounts of dust  
42 and create a propagating dust wall extending up to 2-3 km in the troposphere (Knippertz et al.,  
43 2009; Solomos et al., 2012). These systems are well known by local populations in desert and arid  
44 areas worldwide due to their devastating impact on visibility and human health (e.g. Schepanski et  
45 al., 2009; Emmel et al., 2010; Dempsey 2014; Pantillon et al., 2016). Haboobs are formed by the  
46 evaporation (and melting) of hydrometeors as they fall through warm, unsaturated air below the  
47 cloud base of convective clouds. The energy required for these phase changes (latent heat)  
48 generates cooled downdrafts. When the downdrafts hit the surface they spread out due to their  
49 enhanced density compared with the ambient air. These convective outflow boundaries are  
50 turbulent and gusty and when they travel over bare soil and desert areas sediment can be lifted,  
51 creating a propagating dust wall. The scale of the processes that participate in the generation of  
52 such atmospheric density currents ranges from synoptic down to mesoscale and local. As a result,  
53 haboobs and their effects in weather and air-quality cannot be resolved by the coarse global model  
54 resolutions (Marsham et al., 2013). Moreover, haboobs are usually generated over remote arid  
55 areas where no in-situ networks are present and in-site dust-storm measurements can only be  
56 obtained during field campaign experiments (e.g. SAharan Mineral dUst experiment (SAMUM) 1 &  
57 2, Ansmann et al., 2011; FENNEC, Ryder et al., 2015). Following these limitations, most of the efforts  
58 for the studying and forecasting of such intense dust episodes rely on passive and active remote  
59 sensing (e.g. Moderate Resolution Imaging Spectroradiometer (MODIS), European Aerosol Research  
60 Lidar Network (EARLINET), Cloud-Aerosol Lidar and Infrared Pathfinder Satellite Observation  
61 (CALIPSO)) and on high resolution modeling simulations. Assimilation of satellite derived Aerosol  
62 Optical Thickness (AOT), has been shown to improve the dust forecasts in global models especially

63 for the long range transport (Benedetti, et al., 2009); however this approach cannot be easily  
64 adopted for the description of haboobs. The reason is that the convective events and the associated  
65 wind gusts are not properly resolved at coarse model resolutions. As a result, assimilating the  
66 satellite AOT over an inaccurate meteorological field does not improve the dust forecast.

67 A variety of studies on haboobs have been performed worldwide. For example Knippertz et al.  
68 (2009); Reinfried et al. (2009); Solomos et al. (2012); Roberts and Knippertz (2014) analyzed the  
69 physical processes that lead in severe haboob formation in Sahara. Bou Karam et al. (2008) showed  
70 the contribution of the east Atlantic monsoon flow and the associated mesoscale convective  
71 systems (MCS) in dust elevation along the Sahel. Vukovic et al. (2014) described the severe  
72 convective dust storm that hit Phoenix Arizona in July 2011. Asian haboobs from the Taklimakan  
73 and Gobi deserts are described and simulated in Takemi (1999, 2005). All these studies agree in the  
74 complexity of the various physical processes at multiple atmospheric scales that govern the  
75 generation and lifetime of these systems. Apart from their devastating effects at local and near  
76 surface scales, such events may also contribute to the free-troposphere dust burden in several  
77 ways: First, entrainment of dust particles in the free troposphere takes place at the turbulent region  
78 of the density current head (Takemi, 2005; Solomos et al., 2012); Second, they trigger secondary  
79 convective cells along their pathways that may evolve to synoptic scale dust events and third, dust  
80 residuals remain aloft after the cold pool declines.

81 The current article is the second part (Part 2) in a series of articles on the September 2015  
82 extraordinary dust storm in Middle East and Eastern Mediterranean. In Part 1, Mamouri et al.  
83 (2016) presented a detailed analysis of remote sensing and in-situ monitoring of the event over  
84 Cyprus. The formation of similar events is not fully understood and we use this unique episode to  
85 elucidate the mechanism of dust production in this understudied region. Therefore EARLINET  
86 measurements over Cyprus along with CALIPSO and MSG observations are used to fine tune the  
87 Regional Atmospheric Modeling System (RAMS) simulations and explain the physical processes that  
88 resulted in this haboob-driven dust storm. We focus our analysis on the first two days of the event  
89 (6 and 7 September 2015) when the extraordinary dust-storm was generated. To the best of our  
90 knowledge this is the first detailed modeling and remote sensing study to describe a Middle East  
91 haboob. The modeling and measurement techniques for the analysis are presented in Section 2.  
92 Section 3 includes the model results, the remote sensing and the investigation of the atmospheric  
93 processes that led in the formation of the dust episode. Conclusive remarks and discussion are

94 presented in Section 4.

## 95 **2. Instruments and models.**

96

### 97 **2.1 Remote sensing**

#### 98 **2.1.1. EARLINET**

99 The lidar station at Limassol (34.7° N, 33° E; 23 m above sea level, a.s.l.) is part of the European  
100 Aerosol Research Lidar Network (EARLINET: Pappalardo et al., 2014). The EARLINET lidar network is  
101 widely used for aerosol characterization and particularly for dust characterization studies (Mona et  
102 al., 2012). Details on the lidar station equipment and the retrieval algorithms are given in Mamouri  
103 et al. (2016). Dust mass concentration profiles are obtained from the dust optical properties  
104 following the methodology proposed by Ansmann et al. (2012).

105

#### 106 **2.1.2. CALIPSO**

107 The Cloud-Aerosol Lidar with Orthogonal Polarization (CALIOP) is the principal instrument on board  
108 the CALIPSO satellite. CALIOP is a standard dual-wavelength (532 and 1064 nm) backscatter lidar,  
109 operating a polarization channel at 532 nm (Winker et al., 2009) and it has been acquiring high-  
110 resolution profiles of the attenuated backscatter signal at 532 and 1064 nm along with polarized  
111 backscatter signal in the visible channel since 2006. After calibration and range correction of the  
112 lidar backscatter signals (Level 1 CALIPSO product), cloud and aerosol layers are identified and  
113 aerosol backscatter and extinction coefficient profiles at 532 and 1064 nm are retrieved as part of  
114 the Level 2 CALIPSO product. The CALIPSO algorithms are described in detail by Winker et al. (2009).  
115 In this study, we utilize L2 version 3 Aerosol and Cloud profiles product at a horizontal resolution of  
116 5 km and vertical resolution of 60 m (in altitudes up to 8 km above sea level). In extreme haboob  
117 events, where the optical signal is very high, it is possible for the algorithm to wrongly attribute a  
118 dust layer as a cloud. In order to address this issue and fully understand the observed scene we use  
119 collocated information derived from MSG-SEVIRI (see sect. 2.1.3). In the two CALIPSO cases used  
120 here, MSG-SEVIRI RGB images confirmed that CALIPSO overpasses was cloud free, hence we classify  
121 both aerosol and cloud categorized CALIPSO observations as aerosol.  
122 Moreover, both of the cases have significantly high particle depolarization ratio values, which is a  
123 signature of pure dust scenes. In order convert the dust extinction coefficient from CALIPSO into  
124 dust mass concentration, we follow the methodology proposed by Ansmann et al. (2012) using the

125 conversion parameter of desert dust that is proposed in Mamouri and Ansmann (2017). For this  
126 case study we use a lidar ratio of 40 sr that is typical for Middle East dust (Mamouri et al., 2013).  
127 The overall uncertainty in the estimated dust mass concentrations is 20-30%.

128

### 129 **2.1.3. MSG-SEVIRI**

130 The Meteosat dust RGB composite is produced from a combination of three infrared channels of  
131 SEVIRI: IR12.0-IR10.8 (red), IR10.8-IR8.7 (green), and IR10.8 (blue). The channel combination and  
132 visualization parameters (Table 1) were chosen to maximize the visual contrast between the hot  
133 desert surface and lofted dust particles (Lensky and Rosenfeld, 2008). During daytime, the hot  
134 desert sand, made up from large quartz particles, appears white/blue due to the large difference in  
135 emissivity of IR10.8 and IR8.7 channels (green), high temperature (blue), and quite large difference  
136 in IR12.0 and IR10.8 channels (red). In contrast, lofted dust plumes with fine quartz particles have  
137 similar values of emissivity at IR10.8 and IR8.7 and this makes dust appear pink or magenta. Deep  
138 cumulonimbus clouds are depicted with red colors, while thick water clouds appear yellow. The RGB  
139 dust product is a very useful tool to qualitatively monitor dust transport events, taking advantage of  
140 the high temporal resolution of SEVIRI observations. The dust RGB product is provided in hourly  
141 intervals by EUMETSAT (European Organization for the Exploitation of Meteorological Satellites)  
142 and is used in this work to monitor the evolution of the dust transport event.

143 In some cases, however, the usefulness of the product can be limited and this should be considered  
144 in the following discussion. First, the visual contrast of dust and the underlying surface is diminished  
145 when the temperature difference of the two is low, e.g. during nighttime. Second, high levels of  
146 columnar water vapor or the presence of the temperature inversion can mask the presence of dust  
147 in the atmosphere (Brindley et al., 2012). Finally, the contrast of dust and the ground can be further  
148 diminished over some type of surfaces e.g. over rocky terrain, due to its high emissivity at the 8.7  
149  $\mu\text{m}$  channel (Banks and Brindley, 2013).

150

## 151 **2.2 Modeling**

### 152 **2.2.1 RAMS-ICLAMS model**

153 For the simulations used in this study we adopt the online coupled atmospheric and air quality  
154 modeling system RAMS-ICLAMS (Pielke et al., 1992; Meyers et al., 1997; Cotton et al., 2003;  
155 Solomos et al., 2011). The Integrated Community Limited Area Modeling System (ICLAMS) is an

156 enhanced version of RAMS6.0 and it has been developed by the Atmospheric Modeling and  
157 Weather Forecasting Group at the University of Athens, Greece. The model is set up in a two-way  
158 nesting configuration. The external domain grid space is set at 12×12 km and the grid space of the  
159 inner domain is set at 4×4 km. A higher resolution (cloud resolving) grid at 2×2 km is nested over the  
160 haboob generation area at Syria-Iraq-Iran-Turkey borders. The locations of the model domains are  
161 shown in Figure 1. The vertical structure of the model consists of 50 sigma-z terrain following levels.  
162 The first model level is at 50 m above ground and the levels stretch from the surface up to 18 km.  
163 The dust emission scheme follows the saltation and bombardment approach (Marticorena and  
164 Bergametti 1995; Spyrou et al., 2010). Wet and dry deposition of dust is formulated following  
165 Seinfeld and Pandis 1998. Mineral dust is represented with a transport mode of eight radii bins  
166 namely 0.15, 0.25, 0.45, 0.78, 1.3, 2.2, 3.8 and 7.1  $\mu\text{m}$ . Sea salt aerosol is also parameterized  
167 following Monahan et al., 1986; Zhang et al., 2005; Leeuw et al., 2000 and Gong et al., 2002, 2003  
168 and it is represented with an accumulated and a coarse mode at 0.18  $\mu\text{m}$  and 1.425  $\mu\text{m}$  in radius  
169 respectively. Dust and sea salt particles interact with the radiative transfer code of the model (Rapid  
170 Radiative Transfer Model (RRTM), Mlawer et al., 1997; Iacono et al., 2000) for the computation of  
171 heating rate fluxes. The formation of cloud condensation nuclei (CCN) and ice nuclei (IN) from dust  
172 and sea salt particles is also included in the model based on the schemes of Fountoukis and Nenes,  
173 2005 and Barahona and Nenes 2009. Initial and boundary conditions are from the NCEP final  
174 analysis dataset (FNL at 1°×1° resolution) and the sea surface temperature is the NCEP operational  
175 SST at 0.5°×0.5°. The convective parameterization scheme of Kain and Fritsch, 1993 (KF) is activated  
176 for the two coarser grids. Assimilation of radiosonde data from the airports of Adana (36.98°N,  
177 35.35°E, 00Z and 12Z), Bet Dagan (32.00°N, 34.81°E, 00Z and 12Z), Diyarbakir (37.54°N, 40.12°E, 00Z  
178 and 12Z), Mafraq (32.36°N, 36.25°E, 21Z) and Nicosia (35.10°N, 33.30°E, 00Z) is also activated to fine  
179 tune the simulations. A series of sensitivity runs with various model configurations (different  
180 physical schemes, assimilation parameters and domain structures) is performed until we conclude  
181 to the optimum setup for the specific simulation.

182

### 183 **2.2.2 Land use changes and activation of dust sources**

184 An accurate representation of dust sources in the region is crucial for understanding this complex  
185 dust event, but this is hampered by seasonal and interannual variability of dust sources together  
186 with recent land cover changes in the region. The original land use database of the model is the

187 USGS Data Base Version 2 which is obtained from 1-km AVHRR data (Advanced Very High Resolution  
188 Radiometer) spanning April 1992 through March 1993. Firstly, this annual-mean dataset cannot  
189 accurately describe the land use and dust sources at the end of the dry season in the Middle East.,  
190 Secondly, the complex interactions of drier climate (Notaro et al., 2015; Cook et al., 2016),  
191 transboundary water managements (Voss et al., 2013), and prolonged conflict (Jaafar and Woertz,  
192 2016) have led to further changes of land use types that are no longer reflected at the model and  
193 this could have a large impact on dust production. The comparison of Landsat 8 natural color and  
194 NDVI imagery between August 2013 and 2015 (Figure 2) reveals large areas of uncultivated fields in  
195 regions of contested borders and exposed river and lake-bed sediments especially around the  
196 Euphrates river, all of which are known to be very efficient dust sources (Prospero et al, 2002;  
197 Ginoux et al., 2012). The impact of the ongoing conflict on land use and vegetation can be further  
198 highlighted in Figure 3, showing the time series of MODIS NDVI in the region around Hawija, Kirkuk  
199 province, Iraq (region B of Fig.2). Agriculture in Hawija is based on a combination of rain-fed and  
200 irrigated fields, in accordance with a rainy and a dry season from November to May and from June  
201 to October respectively. The NDVI time series clearly captures this behavior, with a major annual  
202 NDVI pick during wet months and a smaller cycle during each summer, probably reflecting the  
203 growth of summer crops with the help of irrigation. This summer cycle is completely absent in 2015.  
204 Indeed, a recent survey of the Food and Agriculture Organization (FAO) of the United Nations,  
205 reveals that large parts of the irrigation system in Kirkuk and surrounding regions have been  
206 destroyed by military operations and a large number of pumps and generators required for  
207 irrigation have been stolen (Singh N. et al, 2016). This, together with the destruction of other  
208 agricultural equipment and infrastructures, has severely disrupted the summer agriculture activities  
209 of 2015, exactly before the dust storm studied here, leaving the fields to act as very efficient dust  
210 sources.

211 In order to get most accurate representation of dust sources for the specific event we use 1km  
212 monthly Normalized Difference Vegetation Index (NDVI) from MODIS (Didan K., 2015) to  
213 characterize land use type in the region of interest. Specifically, we consider regions with NDVI  
214 values from 0 to 0.1 to correspond to bare soil and consequently efficient dust sources (DeFries et  
215 al., 1994). The updated land cover dataset is used for all results shown in this study. Results from  
216 simulations using the older database are only shown in Figure 11 for comparison.

217



218

### 219 **3. Results**

#### 220 **3.1 Meteorological conditions**

221 The main driving force for the generation of this extreme dust episode is the combination of two  
222 distinct meteorological features in the greater area: (i) establishment of a thermal low over the  
223 bare-soil areas of Syria and (ii) convective outflow boundaries at the mountains of Iraq and Syria.  
224 These processes are analyzed in the following sections using modeling results and remote sensing.

225

##### 226 **3.1.1 Development of a low pressure system over Syria on 6 September 2015**

227 As seen at the outer model grid in Figure 4a, the passage of a trough is evident over Turkey on 6  
228 September 2015, 00:00 UTC. The low pressure center at 500 mb is found at 5840 m over the east  
229 bank of Black Sea. During the same day, radiative warming of the bare soil surface results in very  
230 hot soil temperatures exceeding 50 °C in Syria and Iraq. Advection of warm air from the Red Sea is  
231 also evident at the lowest troposphere by the 1000-700 mb thickness in Figure 4b. This combination  
232 of cold air aloft with low level warming, leads in the formation of a thermal low pressure system  
233 over Syria that is evident by the 925 mb geopotential height in Figure 4c. Another parameter that  
234 plays important role for the process of dust source activation is the difference between surface  
235 temperature ( $T_{\text{surf}}$ ) and air temperature at 2m ( $T_{2\text{m}}$ ). Findings from earlier field experiments (i.e.  
236 SAMUM) show that such a difference of 17°C-20°C facilitates the uplift of convective dust plumes  
237 (Ansmann et al., 2009). As seen in Figure 1, the modeled  $T_{\text{surf}}-T_{2\text{m}}$  difference at 10:00 UTC exceeds  
238 17°C over extended bare soil areas in Syria. This temperature gradient further explains the  
239 effectiveness of dust production at these areas. The pressure system and the associated cyclonic  
240 flow persist during the entire day of 6 September 2015 and result in the mobilization of dust in the  
241 area. Dust uptake is mostly evident at the outer parts of the cyclone where surface wind speed  
242 exceeds  $7 \text{ m s}^{-1}$  almost during the entire day and  $T_{\text{surf}}-T_{2\text{m}}$  obtains maximum values. The elevated  
243 particles are quickly distributed inside the system and a distinct cylindrical dust cloud is soon  
244 formed. Recirculation of the elevated dust particles inside the closed cyclonic flow results in  
245 extreme AOT values exceeding 15 at specific areas as seen in Figure 4c. The formation of this dense  
246 dust plume is also evident in the MSG-SEVIRI satellite dust RGB image in Figure 4d. Pink and purple  
247 colors in this image indicate dust while brown and red colors indicate clouds. The convective  
248 outflows from the Zagros Mountains in Turkey that are evident by the black dashed line and wind



249 vectors at 925 mb in Figure 4c enhance the mobilization of dust at the northern parts of the heat  
250 low. Transport of dust from Lebanon towards Cyprus is evident at the satellite and modeling  
251 images on 7 September 2015, 00:00 UTC (Figure 5). This cut-off plume (plume\_1) travels in the  
252 lower troposphere above the marine boundary layer and it was observed at 1.5 km above Limassol  
253 on 7 September, 19:00 UTC as reported by Mamouri et al. (2016). The faster propagating haboob  
254 plume (plume\_2) was detected at 2.0-3.5 km over Cyprus at 19:00 UTC. The extreme AOT values  
255 (>10) that are seen in Figure 5a over Syria result from the overlapping of cyclone-driven and  
256 haboob-driven dust over this area. In the model, approach of the haboob front in Syria is  
257 accompanied also by cloud formation as seen by the 70% cloud-cover contours in Figure 5a;  
258 however these clouds are not evident in the satellite image (Figure 5b). The more elevated (cyclone-  
259 driven) dust in Figure 5b is shown in pink (plume\_1 over the sea and plume\_3 over Northern Syria  
260 and Southern Turkey) and the near surface dust (haboob) is shown with a darker purple color  
261 (plume\_2).

### 262 263 **3.1.2. Convection and haboob generation on 6 and 7 September 2015**

264 At 13:00 UTC on 6 of September a northward low level flow is evident over N. Iraq and N. Syria  
265 (Figure 6a). This relatively unstable air mass is characterized by increased equivalent potential  
266 temperature ( $\theta_e$ ) reaching up to 508 K. This flow is associated with a westerly shift of the  
267 Somalian Low Level Jet (SLLJ). The SLLJ is part of the West India Monsoon circulation and is shown in  
268 Figure 6b. It is characterized by strong SW winds blowing from the Somali highlands towards West  
269 India. This low level flow steers towards the west along the coastal mountains of Yemen and Oman  
270 and results in SE winds transferring moisture from the Arabian Sea towards the inlands of the  
271 Arabian Peninsula. Low-level advection of warm air masses from the Red Sea and Saudi Arabia  
272 towards the storm area is also evident in Figure 6c by the 1000-700 mb modeled thickness at 15:00  
273 UTC. Mechanical elevation of this relatively unstable air as it approaches Mt. Sinjar in N. Iraq  
274 triggers convection at this area. A number of atmospheric parameters that determine the formation  
275 of the cold pool are shown in Figures 7a-d. As seen in Figure 7a, the iso-temperature line of  $-20^{\circ}\text{C}$   
276 between rain droplets and ambient air temperature clearly defines the cold pool area. Sub-  
277 saturated air below the cloud base is also evident in Figure 7a since the relative humidity at the  
278 neighbor of the convective cloud is between 15-20 %. The combination of sub-saturated air and  
279 temperature gradient results in a faster evaporation rate of the rain droplets and in the formation

280 of a cold pool at the area of Northern Iraq with speeds ranging from 10 up to 20  $\text{ms}^{-1}$  (Figure 7b). As  
281 seen in Figure 7c, the convective cloud top reaches 12 km and the updrafts exceed 18  $\text{m s}^{-1}$  at 15:00  
282 UTC. The rainfall curtain (downdraft area in Figure 7c) extends up to 4-5 km and the severity of the  
283 storm leads in the formation of a haboob that is evident by the streamline structure and dust  
284 production below the non-precipitating parts of the cloud in Figure 7d. A Kelvin-Helmholtz billow at  
285 2-3 km separates the density current head from the ambient flow similar to previous findings for  
286 convective haboobs (Solomos et al., 2012). Turbulence distributes the dust particles inside the  
287 system and dust concentrations exceed 2000  $\mu\text{g m}^{-3}$  close to the surface. As the cold pool moves  
288 towards the North it triggers the generation of secondary convective cells at the mountainous areas  
289 along Iran-Iraq-Turkey borderline. At 20:00 UTC, a series of convective outflows converges in an  
290 organized SE propagating density current that is evident in the model over N. Iraq and N. Syria  
291 (Figure 8a). This system is characterized by wind speeds higher than 6  $\text{m s}^{-1}$  and results in activation  
292 of dust sources and near surface modelled concentrations largely exceeding 10000  $\mu\text{g m}^{-3}$  (Figure  
293 8b). However, the corresponding SEVIRI image (Figure 8c) indicates that by this time the haboob has  
294 already penetrated about 200 km inside Syria which is not reproduced by the model. The latency  
295 between satellite and modeled haboob fronts is possibly attributed to a slower propagating  
296 modeled haboob or to a triggering delay of convection in the model due to the imperfect  
297 representation of boundary layer properties and atmospheric stability.

298

## 299 **3.2 Dust cloud properties and comparison with observations**

### 300 **3.2.1. Vertical dust structure**

301 The dust layer structure as it propagates towards the Mediterranean is captured by two CALIPSO  
302 overpasses at 23:33 UTC, 6 September 2015 (Figure 9) and at 10:35 UTC, 7 September 2015 (Figure  
303 10). Collocated model cross sections of dust and MSG-SEVIRI dust images are also presented in  
304 Figures 9 and 10. All heights in satellite and model profiles refer to heights above surface. At the 6  
305 September overpass, the southern part of the dust layer (31°N-34°N) is detected up to 2-3 km and  
306 originates from the cyclonic flow over Syria (Figure 9c). The modeled dustload is also shown in  
307 Figure 9b for comparison. Dust concentrations are estimated from CALIOP lidar backscatter signals  
308 (see Section 2.1.2) and as seen in Figure 9c they reach up to 5000  $\mu\text{g m}^{-3}$  close to the surface  
309 between 31°N-34°N and higher than 6000  $\mu\text{g m}^{-3}$  in the first 500 m. Similar structure and dust  
310 concentrations are also found by the model (Figure 9d). The northern part of the overpass (35°N-

311 38°N) detects also elevated dust due to cyclonic activity between 2.5-4.5 km and concentrations up  
312 to 1000-2000  $\mu\text{g m}^{-3}$  are evident at this area from CALIPSO. The model overpredicts dust at this area  
313 with simulated concentrations reaching up to 5000  $\mu\text{g m}^{-3}$ . These elevated layers are shown with  
314 pink colors in Figure 9a. Low level dust (purple colors in SEVIRI images) is also evident in this area  
315 due to the propagating haboob and CALIPSO detects this two-layer structure with a clear separation  
316 at 2 km. The model also reproduces the uplift of dust at 35°N where the two systems (cyclone and  
317 haboob) merge. The modeled concentration inside the haboob reaches extraordinary values  
318 exceeding 10000  $\mu\text{g m}^{-3}$ . Due to the severity of the event, the CALIPSO lidar signal is totally  
319 attenuated below  $\sim 1$  km (dark blue color), in the area between 35°N-37°N. For that reason the  
320 information from the satellite is limited at this area in the top 500m of the propagated haboob (1-  
321 1.5 km), implying also the existence of much higher values close to the surface.

322 The second overpass at 7 September 10:35 UTC is actually behind or at the tail of the propagating  
323 dust storm (Figure 10a). The modeled dustload is also shown in Figure 10b for comparison. The thin  
324 dust layer that is detected by CALIPSO between 30°N-32°N reaches up to 2 km and maximum dust  
325 concentrations of up to 2000-3000  $\mu\text{g m}^{-3}$  are calculated mostly close to the surface (Figure 10c).  
326 Extreme dust concentrations are also found in both satellite (Figure 10c) and model plots (Figure  
327 10d) between 34°N-36°N at the tail of the propagating system. Dust values at this area are so high  
328 that CALIPSO observation again suffers from total attenuation of the lidar signal after penetrating  
329 the first 1000 m and extraordinary concentrations of up to 20000  $\mu\text{g m}^{-3}$  are found in the lower  
330 model levels (up to 1.5 km). Similar values are observed from CALIPSO at the edge of the haboob  
331 (33.5°N-34°N) where the signal is strong enough to provide valuable information. The elevated  
332 layers (2-4 km) between 36°N-38°N at both CALIPSO and model profiles are dust residuals over the  
333 mountains of Turkey. An elevated dust layer of up to 600  $\mu\text{g m}^{-3}$  is also found south of 35°N in the  
334 model at heights between 3-4 km. Due to the aforementioned latency between the true and  
335 modeled propagation speeds, the model cross-section is closer to the core of the system hence this  
336 layer consists of modeled cyclone uplifted dust that in fact is already west of the CALIPSO ground  
337 track.

338

### 339 **3.2.2. Dust load over Cyprus**

340 The observed structure and amounts of dust arriving in Cyprus is described in detail by Mamouri et  
341 al. (2016). The arrival of the dust plumes at Limassol in Cyprus is evident in Figure 11. A double layer

342 structure is detected by the lidar on 7 September 19:00 UTC. The relatively shallow dust layer that is  
343 found between 0.8-1.7 km with a maximum peak at  $2000 \mu\text{g m}^{-3}$ , comes from the detached dust air  
344 mass traveling off the coast of Lebanon as described in Section 3.1.1. The model reproduces  
345 correctly the height of this layer but the maximum concentration is underestimated by almost 50 %.  
346 The upper layer that is detected between 1.8-3.6 km originates from the north part of the fast  
347 propagating haboob that catches up with the “Lebanon” dust over Cyprus. The location and dust  
348 concentrations of this layer are adequately reproduced by the model. The total modeled dust load  
349 is similar to the observed (lidar) dust load but the vertical distribution of dust in two distinct layers  
350 is not so clearly reproduced. Model results using the old vegetation database are also shown in  
351 Figure 11. As seen by the dashed line in this plot, this simulation failed to reproduce the strength of  
352 the event and the maximum concentration is  $400 \mu\text{g m}^{-3}$  at about 0.7 km height. On 8 September  
353 the lidar system could not operate due to the extraordinary dust load. The mean MODIS derived  
354 AOT on this day varied between 1.5-5 over five sites in Cyprus (Pafos, Limassol, Larnaca, Nicosia,  
355 Rizokarpaso), (Mamouri et al., 2016). Given the fact that the maximum retrievable MODIS AOT is 5,  
356 these values are most probably an underestimation of the true AOT. The distribution of modeled  
357 AOT during 00:00 UTC-15:00 UTC on 8 September is shown in Figure12; the dust plume approaches  
358 Cyprus from the South and the orographic effect of Mt. Troodos results in an inhomogeneous  
359 distribution of dustload over the island, which explains the AOT variability between the sites. The  
360 modeled AOT values over the Middle East inland exceed 10 as shown also by the sharp gradient  
361 towards the eastern part of Figure 12 plots. However the extreme dust storm affecting Cyprus  
362 during 8 September is the result of a plume that approaches the island from the south. This dust  
363 layer is evident between 1.5-3.5 km in the vertical cross-sections of model dust concentration at  
364 00:00 UTC and 03:00 UTC in Figure 13. Differential heating between the land and water bodies and  
365 between flat terrain and mountain slopes results in the development of local wind flows  
366 (downslope / upslope winds). Downward mixing of dust as this air mass approaches the topographic  
367 barrier of Troodos mountain increases the near-surface concentrations at the southern sites  
368 especially during local morning and noon hours (06:00 UTC, 09:00 UTC). In the afternoon hours  
369 (12:00 UTC, 15:00 UTC), the development of upward motions over Mt. Troodos separates the dust  
370 flow over Cyprus into two distinct cells (a south and a north one) and at this time increased  
371 concentrations are found over the northern sites of the island. The maximum simulated  
372 concentrations are up to  $4000 \mu\text{g m}^{-3}$  aloft and about  $1000 \mu\text{g m}^{-3}$  close to the surface.

373 Taking into account the complexity of the situation, the spatiotemporal evolution of the episode  
374 seems to be correctly explained by the model but the extreme values of 8000-10000 mg m<sup>-3</sup> that  
375 are reported by Mamouri et al. (2016) are not reproduced. This discrepancy can be attributed to a  
376 variety of reasons related to both dust and atmospheric properties that are not properly resolved at  
377 this model scale (e.g. more intense downward mixing, increased emissions from the sources,  
378 limitations due to emission size bins, inaccurate deposition rates etc.). The simulated versus  
379 observed maximum AOT values for the five sites are also shown in Table 2. The model reproduces  
380 the higher AOTs at the most southern sites (Limassol and Pafos) compared to the central and north  
381 sites. Following the previous discussion about the already underestimated MODIS AOT it seems that  
382 the model reproduces the distribution of dust over Cyprus however with an overall underestimation  
383 of more than 2. A possible explanation could be also that the dry river beds of Tigris and Euphrates  
384 as well as several dust sources over Syria and North Iraq provide even more erodible sediments  
385 than those assumed by the model hence the discrepancies in dust concentrations.

386

#### 387 **4. Discussion and Conclusions**

388 A combination of meteorological and land-use conditions resulted in the formation of an  
389 unprecedented dust episode over Middle East and the Eastern Mediterranean during 6-11  
390 September 2015. This event is unique due to the coincidence of various atmospheric phenomena  
391 related with the generation of turbulence and dust production. Interpretation and analysis of  
392 remote sensing data (EARLINET, CALIPSO, MSG-SEVIRI) and modeling simulations (RAMS-ICLAMS)  
393 reveals the main reasons that led in the uplift and persistence of the dust layers.

394 The major processes affecting the generation of the dust storm are found to be:

- 395 1. The formation of a strong thermal low and of convective outflows over Syria that lifted dust  
396 up to 4 km.
- 397 2. The intrusion of moist and unstable air masses from the Arabian Sea and the Red Sea that  
398 triggered convective activity over Iraq-Iran-Syria-Turkey borderline.
- 399 3. The generated outflow boundaries that led in dust deflation and formed a westward  
400 propagating haboob merging with the previously elevated dust over Syria.
- 401 4. The increased efficiency of Middle East dust sources as an aftermath of war and the related  
402 changes in land use.

403 As reported by Mamouri et al. (2016), almost all operational dust models failed to forecast this  
404 event. RAMS-ICLAMS in this study is not used in forecasting mode but rather as a tool for the a-  
405 posteriori analysis and explanation of the event. This means that the configuration of several model  
406 parameters such as the nested grid structure, convective parameterization schemes, dust source  
407 strength etc. is guided by the available observations. In this context, most observed processes are  
408 successfully described by the model and the various physical mechanisms that took place during the  
409 event are explained. However, certain inaccuracies in the quantification of atmospheric variables  
410 and spatiotemporal deviations in the description of convection and other physical processes can still  
411 significantly decrease the model skill especially regarding the quantification of dust mass profiles.

412 The analysis presented here raises considerations regarding the forecast skill of the atmospheric  
413 dust models, since even though such extreme episodes are seldom they still represent the most  
414 threatening dust hazards. The long range transport and the general circulation of dust in the  
415 atmosphere are now often adequately forecasted by most global models but convectively driven  
416 episodes cannot be resolved at synoptic and mesoscale resolutions. Moreover, a recent study by  
417 Pope et al. (2016) at the area of Sahel / southern Sahara suggests that unresolved haboobs during  
418 the summer monsoon may be responsible for up to 30% of the total atmospheric dust and such  
419 considerations raise questions on the current status of early warning systems for dust episodes. It is  
420 probably obvious that such a system cannot rely exclusively on modeling simulations. As shown at  
421 the present study, the complexity of these events makes forecasting them very challenging and it is  
422 possible that a certain model configuration could successfully reproduce a specific event but not all  
423 similar events. The key for forecasting these events in atmospheric models is the use of cloud  
424 resolving grid space. However, such high resolution grid-space can only be applied over limited  
425 areas due to restrictions in computational power. Forthcoming studies using an extended cloud-  
426 resolving grid over the entire Middle-East (e.g. Gasch et al., 2017) could provide more detail on the  
427 individual atmospheric processes during this episode.

428 Remote sensing can play an important role for the provision of more accurate dust forecasts.  
429 Engagement of geostationary satellite observations (MSG, Sentinel-4) and CALIPSO profiles in  
430 forecasting activities could improve the forecasting skill either by the direct assimilation of satellite  
431 data in dust models or by issuing human-assisted early warnings. Expansion of a lidar network close  
432 to dust source areas (e.g. Sahara, Middle East) will also complement model activities through the  
433 provision of ground truth observations for the vertical profile of dust plumes. Additionally, the

434 activation of correlated observations from the EARLINET network following a dust forecast notice  
435 will allow a closer investigation of the physical processes that drive these events.

436

437

#### 438 **Acknowledgements**

439 The authors acknowledge support through the following projects and research programs: BEYOND  
440 under grant agreement no. 316210 of the European Union Seventh Framework Programme FP7-  
441 REGPOT-2012-2013-1. ACTRIS-2 under grant agreement no. 654109 of the European Union's  
442 Horizon 2020 research and innovation programme. ECARS under grant agreement No 602014 from  
443 the European Union's Horizon 2020 Research and Innovation programme. MarcoPolo under grant  
444 agreement no. 606953 of the European Union Seventh Framework Programme FP7/2007-2013. The  
445 authors acknowledge EARLINET for providing aerosol lidar profiles available under the World Data  
446 Center for Climate (WDCC) (The EARLINET publishing group 2000-2010, 2014a. CALIPSO data were  
447 obtained from the ICARE Data Center (<http://www.icare.univ-lille1.fr/>) and from the NASA Langley  
448 Research Center Atmospheric Science Data Center. CALIPSO data were provided by NASA. We thank  
449 the ICARE Data and Services Center for providing access to the data used in this study and their  
450 computational center.

451

#### 452 **References**

- 453 Ansmann A., Tesche, M., Knipperts, P., Bierwirth, E., Althausen, D., Müller, D. and Schulz, O.: Vertical profiling  
454 of convective dust plumes in southern Morocco during SAMUM. *Tellus* 61B, doi:10.1111/j.1600-  
455 0889.2008.00384.x., 2009
- 456 Ansmann, A., Petzold, A., Kandler, K., Tegen, I., Wendisch, M., Müller, D., Weinzierl, B., Müller, T., and  
457 Heintzenberg, J.: Saharan Mineral Dust Experiments SAMUM-1 and SAMUM-2: what have we learned?,  
458 *Tellus*, 63B, 403–429, 2011
- 459 Ansmann, A., Seifert, P., Tesche, M., and Wandinger, U.: Profiling of fine and coarse particle mass: case  
460 studies of Saharan dust and Eyjafjallajökull/Grimsvötn volcanic plumes, *Atmos. Chem. Phys.*, 12, 9399–  
461 9415, doi:10.5194/acp-12-9399-2012, 2012.
- 462 Banks, J. R. and Brindley, H. E.: Evaluation of MSG-SEVIRI mineral dust retrieval products over North Africa  
463 and the Middle East, *Remote Sensing of Environment*, 128, 58–73, doi:10.1016/j.rse.2012.07.017, 2013.
- 464 Barahona, D., West, R. E. L., Stier, P., Romakkaniemi, S., Kokkola, H., and Nenes, A.: Comprehensively  
465 accounting for the effect of giant CCN in cloud activation parameterizations, *Atmos. Chem. Phys.*, 10,  
466 2467–2473, doi:10.5194/acp-10-2467-2010, 2010.



467 Benedetti A., J.-J., Morcrette, O. Boucher, A. Dethof, R. J. Engelen, M. Fisher, H. Flentje, N. Huneeus, L. Jones,  
468 J. W. Kaiser, S. Kinne, A. Mangold, M. Razinger, A. J. Simmons, and M. Suttie: Aerosol analysis and forecast  
469 in the European Centre for Medium-Range Weather Forecasts Integrated Forecast System: 2. Data  
470 assimilation, *J. Geophys. Res.*, 114, D13205, doi:10.1029/2008JD011115., 2009

471 Bou Karam, D., Flamant, C., Knippertz, P., Reitebuch, O., Pelon, J., Chong, M., and Dabas, A: Dust emissions  
472 over the Sahel associated with the West African Monsoon inter-tropical discontinuity region: a  
473 representative case study, *Q. J. Roy. Meteor. Soc.*, 134, 621–634, 2008.

474 Brindley, H., Knippertz, P., Ryder, C. and Ashpole, I.: A critical evaluation of the ability of the Spinning  
475 Enhanced Visible and Infrared Imager (SEVIRI) thermal infrared red-green-blue rendering to identify dust  
476 events: Theoretical analysis, *J. Geophys. Res.*, 117(D7), D07201, doi:10.1029/2011JD017326, 2012.

477 Cook, B. I., Anchukaitis, K. J., Touchan, R., Meko, D. M. and Cook, E. R.: Spatiotemporal drought variability in  
478 the Mediterranean over the last 900 years, *J. Geophys. Res. Atmos.*, 121(5), 2015JD023929,  
479 doi:10.1002/2015JD023929, 2016.

480 Cotton W. R., Pielke Sr., R. A., Walko, R. L., Liston, G. E., Tremback, C. J., Jiang, H., McAnelly, R. L., Harrington,  
481 J. Y., Nicholls, M. E., Carrio, G. G., and McFadden, J. P.: RAMS 2001: Current status and future directions,  
482 *Meteor. Atmos. Phys.*, 82, 5–29, 2003

483 DeFries, R. S. and Townshend, J. R. G.: NDVI-derived land cover classifications at a global scale, *International*  
484 *Journal of Remote Sensing*, 15(17), 3567–3586, doi:10.1080/01431169408954345, 1994.

485 Dempsey M. J., “Forecasting Strategies for Haboobs: An Underreported Weather Phenomenon,” *Advances in*  
486 *Meteorology*, vol. 2014, Article ID 904759, 6 pages, 2014. doi:10.1155/2014/904759

487 Didan, K: MOD13A3 MODIS/Terra vegetation Indices Monthly L3 Global 1km SIN Grid V006, ,  
488 doi:10.5067/MODIS/MOD13A3.006, 2015.

489 Emmel C, Knippertz P, Schulz O (2010) Climatology of convective density currents in the southern  
490 foothills of the Atlas mountains. *J Geophys Res* 115, D11115. doi:10.1029/2009JD011819

491 Fountoukis, C., Nenes, A., Meskhidze, N., Bahreini,, R., Conant, W. C., Jonsson, H., Murphy, S., Sorooshian, A.,  
492 Varutbangkul, V., Brechtel, F., Flagan, R. C., and Seinfeld, J. H.: Aerosol – cloud drop concentration closure  
493 for clouds sampled during the International Consortium for Atmospheric Research on Transport and  
494 Transformation 2004 campaign, *J. Geophys. Res.*, 112, D10S30, doi:10.1029/2006JD007272, 2007.

495 Gasch, P., Rieger, D., Walter, C., Khain, P., Levi, Y., and Vogel, B.: An analysis of the September 2015 severe  
496 dust event in the Eastern Mediterranean, *Atmos. Chem. Phys. Discuss.*, doi:10.5194/acp-2017-11, in  
497 review, 2017.

498 Ginoux, P., Prospero, J. M., Gill, T. E., Hsu, N. C. and Zhao, M.: Global-scale attribution of anthropogenic and  
499 natural dust sources and their emission rates based on MODIS Deep Blue aerosol products, *Rev.*  
500 *Geophys.*, 50(3), RG3005, doi:10.1029/2012RG000388, 2012.

501 Gong, S. L., Barrie, L. A., and Lazare, M.: Canadian Aerosol Module (CAM): a size-segregated simulation of

502 atmospheric aerosol processes for climate and air quality models. 2. Global seasalt aerosol and its  
503 budgets, *J. Geophys. Res.*, 107(D24), 4779, doi:10.1029/2001JD002004, 2002.

504 Gong, S. L.: A parameterization of sea-salt aerosol source function for sub- and super-micron particles, *Global*  
505 *Biogeochem. Cy.*, 17, 1097, doi:10.1029/2003GB002079, 2003.

506 Iacono, M. J., Mlawer, E. J., Clough, S. A., and Morcrette, J. J.: Impact of an improved longwave radiation  
507 model, RRTM, on the energy budget and thermodynamic properties of the NCAR Community Climate  
508 Model, CCM3, *J. Geophys. Res.*, 105, 14873–14890, 2000

509 Jaafar, H. H. and Woertz, E.: Agriculture as a funding source of ISIS: A GIS and remote sensing analysis, *Food*  
510 *Policy*, 64, 14–25, doi:10.1016/j.foodpol.2016.09.002, 2016.

511 Kain, J. S. and Fritsch, J. M.: Convective parameterization for mesoscale models: The Kain-Fritsch scheme. The  
512 representation of cumulus convection in numerical models, *Meteor. Monogr.*, No. 24, Amer. Meteor.  
513 Soc., 165–170, 1993.

514 Knippertz P, Trentmann J. Seifert A., High resolution simulations of convective cold pools over the  
515 northwestern Sahara. *J. Geophys. Res.* 2009; 114:D21109. doi: 10.1029/2007JD008774., 2009

516 Leeuw, G., Neele, F. P., Hill, M., Smith, M. H., and Vignali, E.: Production of sea spray aerosol in the surf zone,  
517 *J. Geophys. Res.- Atmos.*, 105, 29397–29409, 2000.

518 Lensky I.M. and D. Rosenfeld, 2008: Clouds-Aerosols-Precipitation Satellite Analysis Tool (CAPSAT). *Atmos.*  
519 *Chem. Phys.*, 8, 6739–6753.

520 Mamouri, R. E., Ansmann, A., Nisantzi, A., Kokkalis, P., Schwarz, A., and Hadjimitsis, D.: Low Arabian dust  
521 extinction-to-backscatter ratio, *Geophys. Res. Lett.*, 40, 4762–4766, doi:10.1002/grl.50898, 2013.

522 Mamouri R.E., Ansmann, A., Nisantzi, A., Solomos, S., Kallos, G., and Hadjimitsis, D.G.: Extreme dust storm  
523 over the eastern Mediterranean in September 2015: satellite, lidar, and surface observations in the  
524 Cyprus region *Atmos. Chem. Phys.*, 16, 1–14, 2016 [www.atmos-chem-](http://www.atmos-chem-phys.net/16/1/2016/)  
525 [phys.net/16/1/2016/](http://www.atmos-chem-phys.net/16/1/2016/)doi:10.5194/acp-16-1-2016.

526 Mamouri, R.E. and Ansmann, A.: Fine and coarse dust separation with polarization lidar: Extended  
527 Methodology for multiple wavelengths, to be submitted to ACP, 2017.

528 Marsham, J. H., N. S. Dixon, L. Garcia-Carreras, G. M. S. Lister, D. J. Parker, P. Knippertz, and C. E. Birch : The  
529 role of moist convection in the West African monsoon system: Insights from continental-scale convection-  
530 permitting simulations, *Geophys. Res. Lett.*, 40, 1843–1849, doi:10.1002/grl.50347., 2013

531 Marticorena, B. and Bergametti, G.: Modeling the atmospheric dust cycle: 1. Design of a soil derived dust  
532 emission scheme, *J. Geophys. Res.*, 100, 16415–16430, 1995.

533 Meyers, M. P., Walko, R. L., Harrington, J. Y., and Cotton, W. R: New RAMS cloud microphysics  
534 parameterization. Part II: The two-moment scheme, *Atmos. Res.*, 45, 3–39, 1997

535 Mlawer, E. J., Taubman, S. J., Brown, P. D., Iacono, M. J., and Clough, S. A.: Radiative transfer for

536 inhomogeneous atmospheres: RRTM, a validated correlated-k model for the longwave, *J. Geophys. Res.*,  
537 102(D14), 16663–16682, 1997.

538 Mona L., Z. Liu, D. Müller, A. Omar, A. Papayannis, G. Pappalardo, N. Sugimoto and M. Vaughan,  
539 “Lidar Measurements for Desert Dust Characterization: An Overview,” *Advances in Meteorology*, vol.  
540 2012, Article ID 356265, 36 pages, 2012. doi:10.1155/2012/356265

541 Monahan, E. C., Spiel, D. E., and Davidson, K. L.: A model of marine aerosol generation via whitecaps and  
542 wave disruption, in: *Oceanic Whitecaps*, edited by: Monahan, E. C. and Mac Niocaill, G., D. Reidel, 167–  
543 174, 1986.

544 Notaro, M., Yu, Y. and Kalashnikova, O. V.: Regime shift in Arabian dust activity, triggered by persistent  
545 Fertile Crescent drought, *J. Geophys. Res. Atmos.*, 120(19), 2015JD023855, doi:10.1002/2015JD023855,  
546 2015.

547 Pappalardo, G., Amodeo, A., Apituley, A., Comeron, A., Freudenthaler, V., Linné, H., Ansmann, A., Bösenberg,  
548 J., D'Amico, G., Mattis, I., Mona, L., Wandinger, U., Amiridis, V., Alados-Arboledas, L., Nicolae, D., and  
549 Wiegner, M.: EARLINET: towards an advanced sustainable European aerosol lidar network, *Atmos. Meas.*  
550 *Tech.*, 7, 2389-2409, doi:10.5194/amt-7-2389-2014, 2014.

551 Pantillon, F., P. Knippertz, J. H. Marsham, H.-J. Panitz, and I. Bischoff-Gauss (2016), Modeling haboob dust  
552 storms in large-scale weather and climate models, *J. Geophys. Res. Atmos.*, 121, 2090–2109,  
553 doi:[10.1002/2015JD024349](https://doi.org/10.1002/2015JD024349).

554 Pielke, R. A., Cotton, W. R., Walko, R. L., Tremback, C. J., Lyons, W. A., Grasso, L. D., Nicholls, M. E., Moran, M.  
555 D., Wesley, D. A., Lee, T. J., and Copeland, J. H.: A comprehensive meteorological modeling system –  
556 RAMS, *Meteorol. Atmos. Phys.*, 49, 69–91, 1992.

557 Pope, R. J., J. H. Marsham, P. Knippertz, M. E. Brooks, and A. J. Roberts: Identifying errors in dust models  
558 from data assimilation, *Geophys. Res. Lett.*, 43, 9270–9279, doi:10.1002/2016GL070621., 2016

559 Prospero, J. M., Ginoux, P., Torres, O., Nicholson, S. E. and Gill, T. E.: Environmental Characterization of  
560 Global Sources of Atmospheric Soil Dust Identified with the Nimbus 7 Total Ozone Mapping Spectrometer  
561 (toms) Absorbing Aerosol Product, *Rev. Geophys.*, 40(1), 1002, doi:10.1029/2000RG000095, 2002.

562 Reinfried, F., I. Tegen, B. Heinold, O. Hellmuth, K. Schepanski, U. Cubasch, H. Huebener, and P. Knippertz :  
563 Simulations of convectively-driven density currents in the Atlas region using a regional model: Impacts on  
564 dust emission and sensitivity to horizontal resolution and convection schemes, *J. Geophys. Res.*, 114,  
565 D08127, doi:10.1029/2008JD010844., 2009

566 Roberts, A. J., P. Knippertz : The formation of a large summertime Saharan dust plume: Convective and  
567 synoptic-scale analysis, *J. Geophys. Res. Atmos.*, 119, 1766–1785, doi:10.1002/2013JD020667., 2014

568 Ryder, C. L., McQuaid, J. B., Flamant, C., Rosenberg, P. D., Washington, R., Brindley, H. E., Highwood, E. J.,

569 Marsham, J. H., Parker, D. J., Todd, M. C., Banks, J. R., Brooke, J. K., Engelstaedter, S., Estelles, V.,  
570 Formenti, P., Garcia-Carreras, L., Kocha, C., Marengo, F., Sodemann, H., Allen, C. J. T., Bourdon, A., Bart,  
571 M., Cavazos-Guerra, C., Chevaillier, S., Crosier, J., Darbyshire, E., Dean, A. R., Dorsey, J. R., Kent, J.,  
572 O'Sullivan, D., Schepanski, K., Szpek, K., Trembath, J., and Woolley, A.: Advances in understanding mineral  
573 dust and boundary layer processes over the Sahara from Fennec aircraft observations, *Atmos. Chem.*  
574 *Phys.*, 15, 8479–8520, doi:10.5194/acp-15-8479-2015, 2015

575 Schepanski, K., Tegen, I., Todd, M. C., Heinold, B., Bonisch, G., Laurent, B., and Macke, A.: Meteorological  
576 processes forcing Saharan dust emission inferred from MSG-SEVIRI observations of subdaily dust source  
577 activation and numerical models, *J. Geophys. Res.*, 114, D10201, doi:10.1029/2008JD010325, 2009.

578 Seinfeld, J. H. and Pandis, S. N.: *Atmospheric Chemistry and Physics: From Air Pollution to Climate Change*, J.  
579 Wiley, New York, 1998

580 Singh N., van Zoonen D., and Khogir M.: Iraq agriculture and livelihoods needs assessment in the newly  
581 liberated areas of Kirkuk, Ninewa and Salahadin, Food and Agriculture Organization of the United Nations,  
582 2016.

583 Solomos, S., Kallos, G., Kushta, J., Astitha, M., Tremback, C., Nenes, A., and Levin, Z.: An integrated modeling  
584 study on the effects of mineral dust and sea salt particles on clouds and precipitation, *Atmos. Chem.*  
585 *Phys.*, 11, 873–892, doi:10.5194/acp-11-873-2011, 2011

586 Solomos, S., Kallos, G., Mavromatidis, E., and Kushta, J.: Density currents as a desert dust mobilization  
587 mechanism, *Atmos. Chem. Phys.*, 12, 11199-11211, doi:10.5194/acp-12-11199-2012, 2012.

588 Spyrou, C., Mitsakou, C., Kallos, G., Louka, P., and Vlastou, G.: An improved limited-area model for describing  
589 the dust cycle in the atmosphere, *J. Geophys. Res.*, 115, D17211, doi:10.1029/2009JD013682, 2010.

590 Takemi, T.: Explicit simulations of convective-scale transport of mineral dust in severe convective weather, *J.*  
591 *Meteorol. Soc. Jpn.*, 83A, 187–203, 2005.

592 Takemi, T.: Structure and evolution of a severe squall line over the arid region in Northwest China. *Mon.*  
593 *Wea. Rev.*, 127, 1301–1309., 1999.

594 The EARLINET publishing group 2000–2010: Adam, M., Alados-Arboledas, L., Althausen, D., Amiridis, V.,  
595 Amodeo, A., Ansmann, A., Apituley, A., Arshinov, Y., Balis, D., Belegante, L., Bobrovnikov, S., Boselli, A.,  
596 Bravo-Aranda, J. A., Bösenberg, J., Carstea, E., Chaikovskiy, A., Comerón, A., D'Amico, G., Daou, D.,  
597 Dreischuh, T., Engelmann, R., Finger, F., Freudenthaler, V., Garcia-Vizcaino, D., García, A. J. F., Geiß, A.,  
598 Giannakaki, E., Giehl, H., Giunta, A., de Graaf, M., Grana-dos-Muñoz, M. J., Grein, M., Grigorov, I., Groß, S.,  
599 ruening, C., Guerrero-Rascado, J. L., Haeffelin, M., Hayek, T., Iarlori, M., Kanitz, T., Kokkalis, P., Linné, H.,  
600 Madonna, F., Mamouri, R.-E., Matthias, V., Mattis, I., Menéndez, F. M., Mitev, V., Mona, L., Morille, Y.,  
601 Muñoz, C., Müller, A., Müller, D., Navas-Guzmán, F., Nemuc, A., Nicolae, D., Pandolfi, M., Papayannis, A.,  
602 Pappalardo, G., Pelon, J., Perrone, M. R., Pietruczuk, A., Pisani, G., Potma, C., Preißler, J., Pujadas, M.,  
603 Putaud, J., Radu, C., Ravetta, F., Reigert, A., Rizi, V., Rocadenbosch, F., Rodríguez, A., Sauvage, L., Schmidt,

604 J., Schnell, F., Schwarz, A., Seifert, P., Serikov, I., Sicard, M., Silva, A. M., Simeonov, V., Siomos, N., Sirch, T.,  
605 Spinelli, N., Stoyanov, D., Talianu, C., Tesche, M., De Tomasi, F., Trickl, T., Vaughan, G., Volten, H., Wagner,  
606 F., Wandinger, U., Wang, X., Wiegner, M., and Wilson, K. M.: EARLINET all observations (2000–2010),  
607 World Data Center for Climate (WDCC), doi:10.1594/WDCC/EN\_all\_measurements\_2000-2010, 2014a.

608 Voss, K. A., Famiglietti, J. S., Lo, M., de Linage, C., Rodell, M. and Swenson, S. C.: Groundwater depletion in  
609 the Middle East from GRACE with implications for transboundary water management in the Tigris-  
610 Euphrates-Western Iran region, *Water Resour. Res.*, 49(2), 904–914, doi:10.1002/wrcr.20078, 2013.

611 Vukovic, A., Vujadinovic, M., Pejanovic, G., Andric, J., Kumjian, M. R., Djurdjevic, V., Dacic, M., Prasad, A. K.,  
612 El-Askary, H. M., Paris, B. C., Petkovic, S., Nickovic, S., and Sprigg, W. A.: Numerical simulation of "an  
613 American haboob", *Atmos. Chem. Phys.*, 14, 3211–3230, doi:10.5194/acp-14-3211-2014, 2014.

614 Zhang, K. M., Knipping, E. M., Wexler, A. S., Bhave, P. V., and Tonnesen, G. S.: Size distribution of sea-salt  
615 emissions as a function of relative humidity, *Atmos. Environ.*, 39, 3373–3379, 2005.

616

617 Table 1. Range and gamma correction for the Red, Green, and Blue channels for construct the Dust  
 618 RGB product.

Color	SEVIRI Channels	Min (K)	Max (K)	$\Gamma$
Red	IR12.0 – IR10.8	-4	2	1
Green	IR10.8 – IR8.7	0	15	2.5
Blue	IR10.8	261	289	1

619

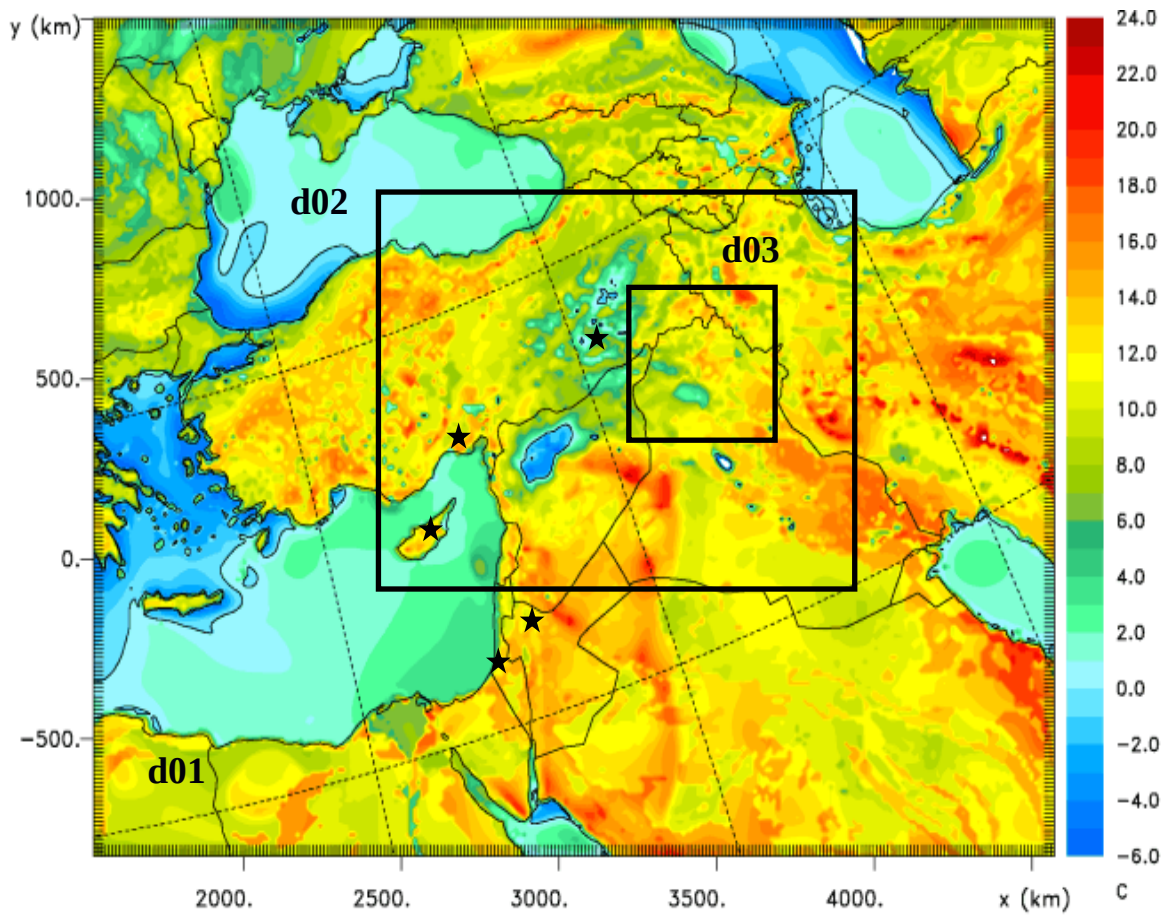
620

621 Table 2. Maximum MODIS and RAMS AOT over Cyprus (8 September 2015)

	Pafos	Limassol	Larnaca	Nicosia	Rizokarpaso
MODIS <sub>AOT</sub>	3.5	5.0	5.0	2.0	5.0
RAMS <sub>AOT</sub>	3.5	4.0	3.0	3.0	3.0

622

623  
624  
625

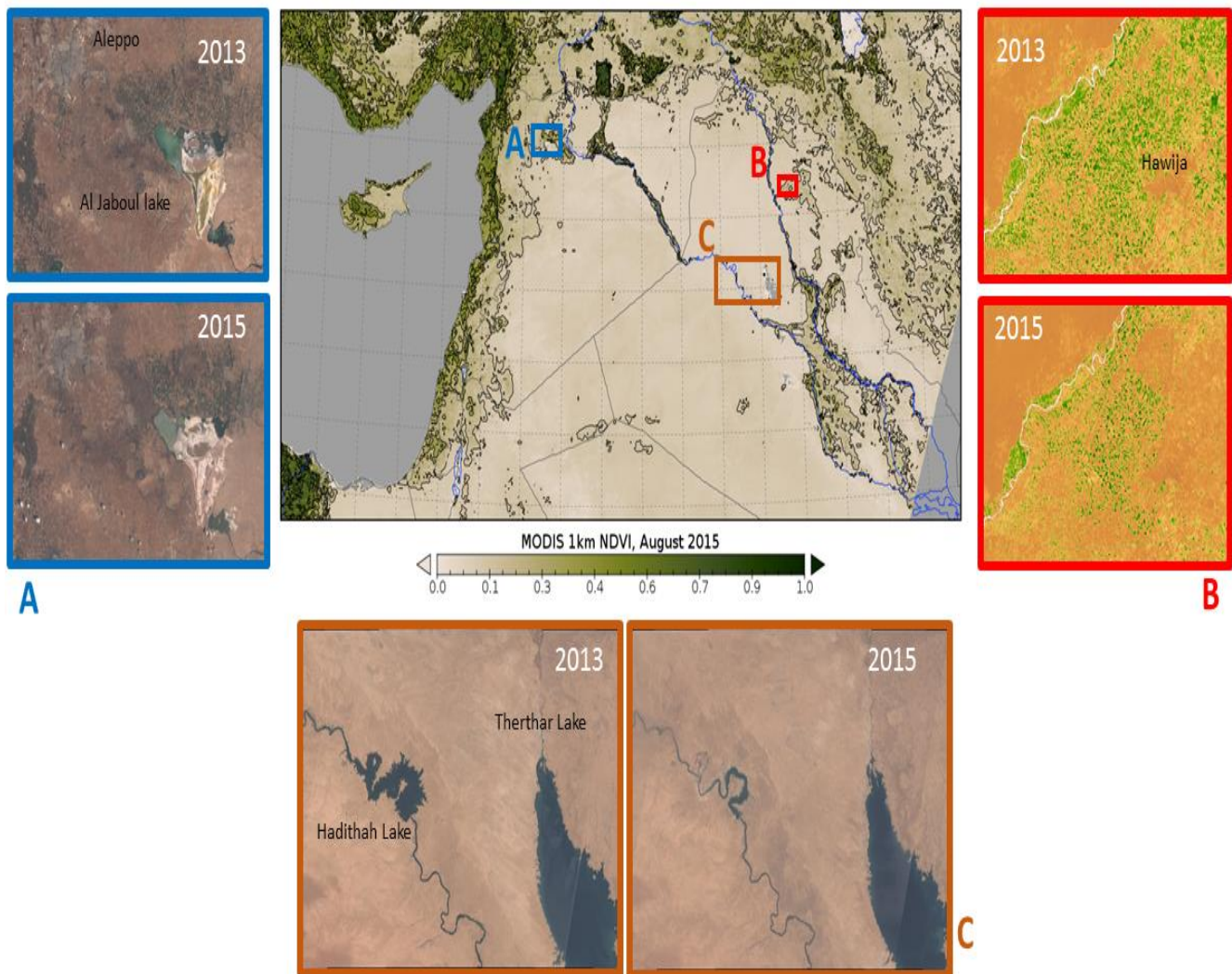


626  
627  
628  
629  
630  
631

Figure 1. Modeling domain structure and difference ( $^{\circ}\text{C}$ ) between model soil temperature and model temperature at 2m, 10:00 UTC, 6 September 2015. Black rectangulars indicate the location of the nested model domains (d01:12 $\times$ 12 km, d02:4 $\times$ 4 km, d03:2 $\times$ 2 km) and black stars the location of radiosondes.

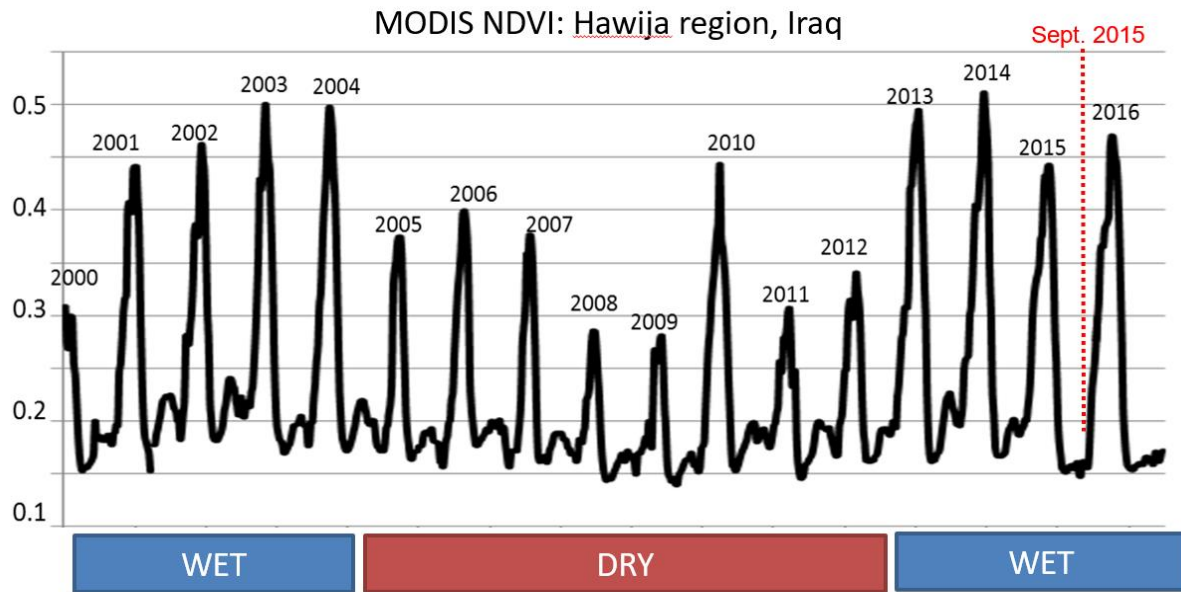


## Land type changes in 2015



632

633 Figure 2. (central panel) MODIS NDVI observations for August 2015 were used to identify regions of  
 634 bare soil that can be sources of dust aerosols. The contour lines correspond to the major ticks of the  
 635 color scale. Large regions of wester Syria and Iraq have NDVI values from 0 to 0.1. The three  
 636 subpanels show examples of land type change between summer 2013 and summer 2015. (Subpanel  
 637 A) Landsat 8 natural color images of Aleppo region, Syria shows changes of cultivation patterns and  
 638 drying of nearby Al Jaboul lake (e.g. the bright areas of the Al Jaboul Lake - dry parts of the lake -  
 639 increased from 2013 to 2015); (Subpanel B) Landsat 8 NDVI index images in the region of Hawija,  
 640 Kirkuk Province, Iraq reveal that large areas remained uncultivated in 2015 (e.g. the 2013 map  
 641 shows many more green spots - agriculturally used areas - than the 2015 map); (Subpanel C)  
 642 Landsat 8 natural color images showing diminishing area of Hadithah Lake on the Euphrates river and  
 643 the drying up of the Therthar canal and lake.

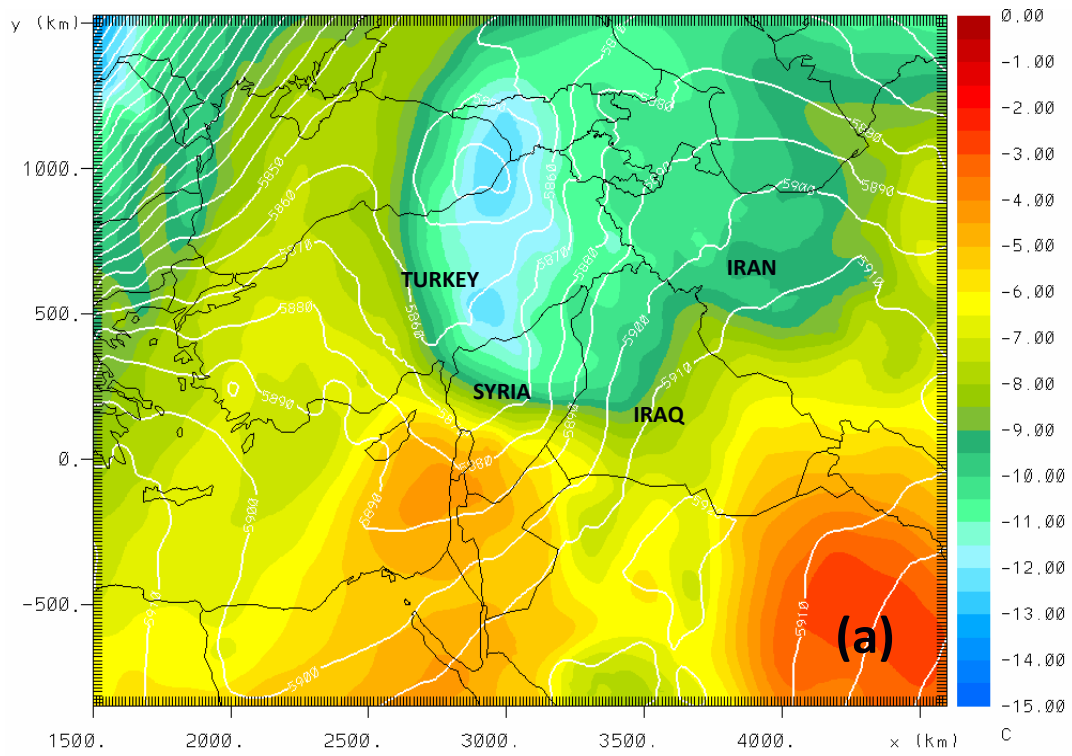


644

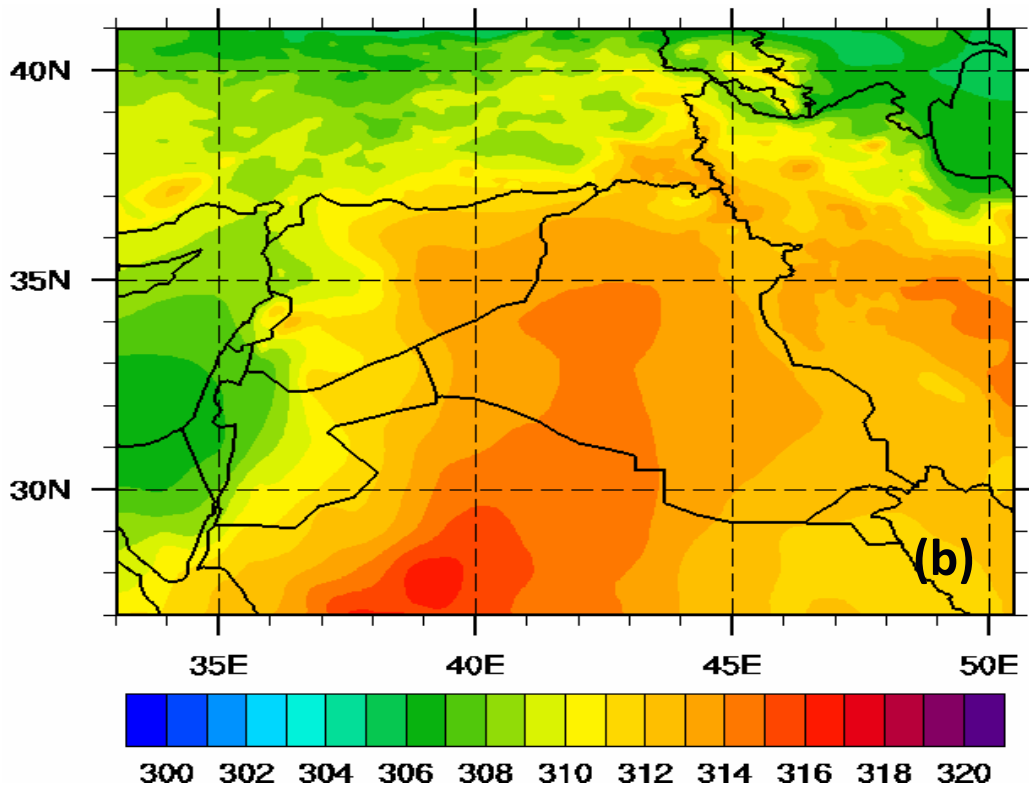
645 Figure 3. Time series of 16-day NDVI for the agricultural region around Hawija, Kirkuk province, Iraq.

646 The vertical dashed lined marks the time of the studied dust storm. Note the absence of NDVI  
 647 variation in the summer of 2015, prior to the dust storm.

648

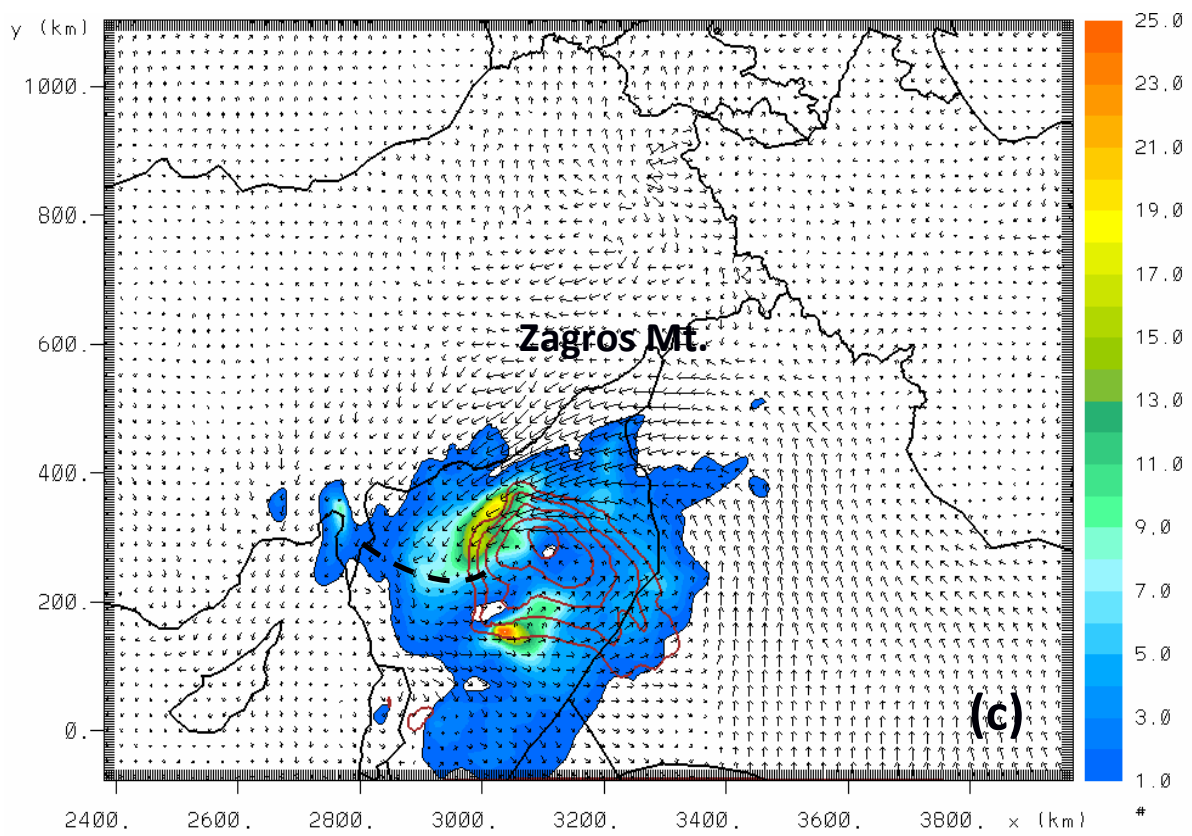


649  
650

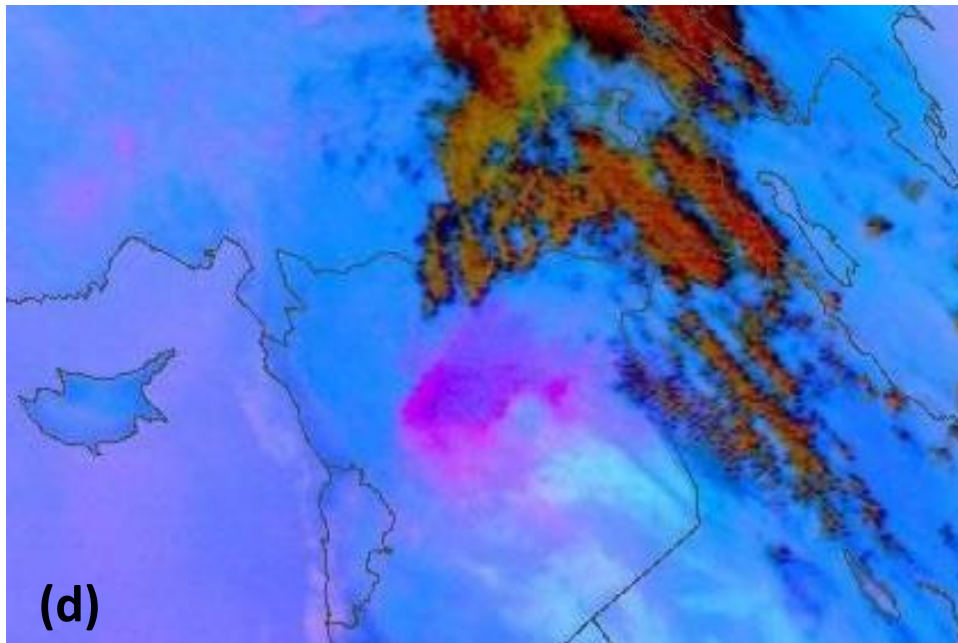


651

652 Figure 4. a) Model geopotential height contours (every 10 m) and temperature (color scale in °C) at  
 653 500mb, 6 September 2015, 00:00 UTC; b) Model 1000-700 mb thickness (dam), 6 September 2015,  
 654 00:00 UTC



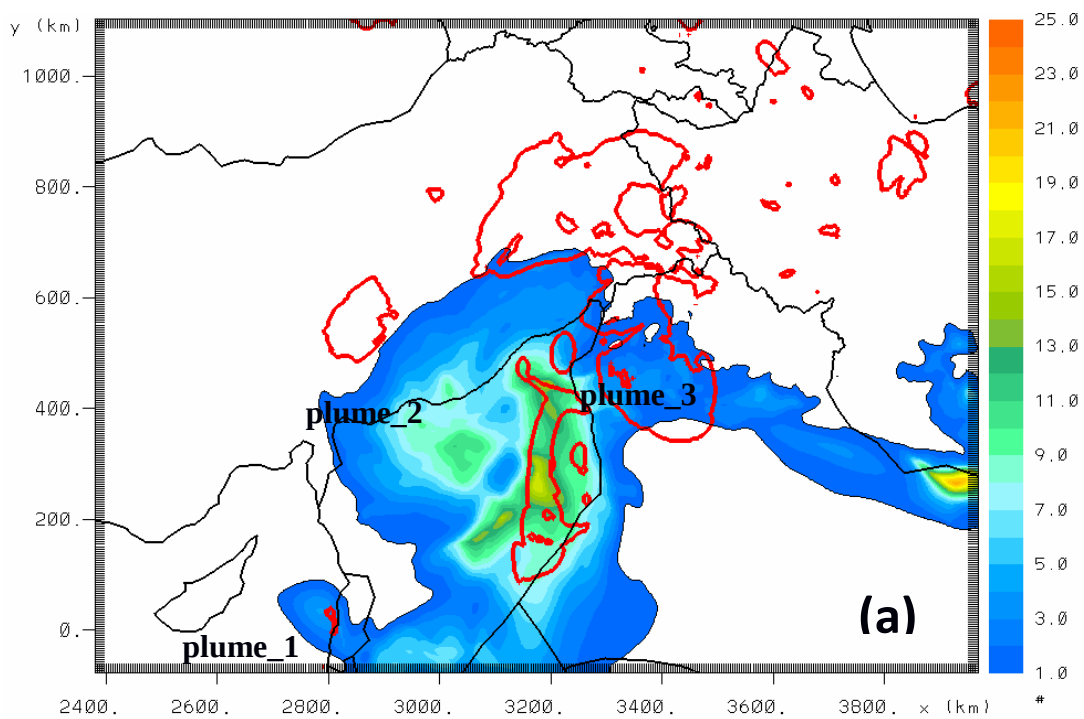
655



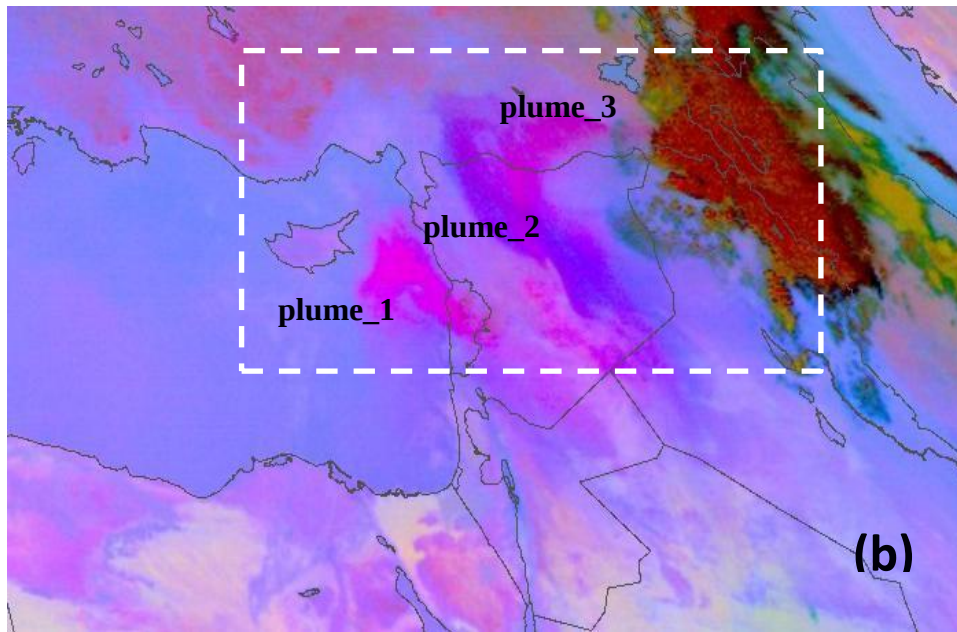
656

657 Figure 4. c) Model AOT (color scale), geopotential height at 925 mb (red contours from 740 to 757.5  
 658 m every 2.5 m) and wind vectors at 925 mb. The dashed line denotes the outflow boundaries from  
 659 Zagros Mountains; d) MSG SEVIRI dust RGB at 08:00 UTC, 6 September 2015



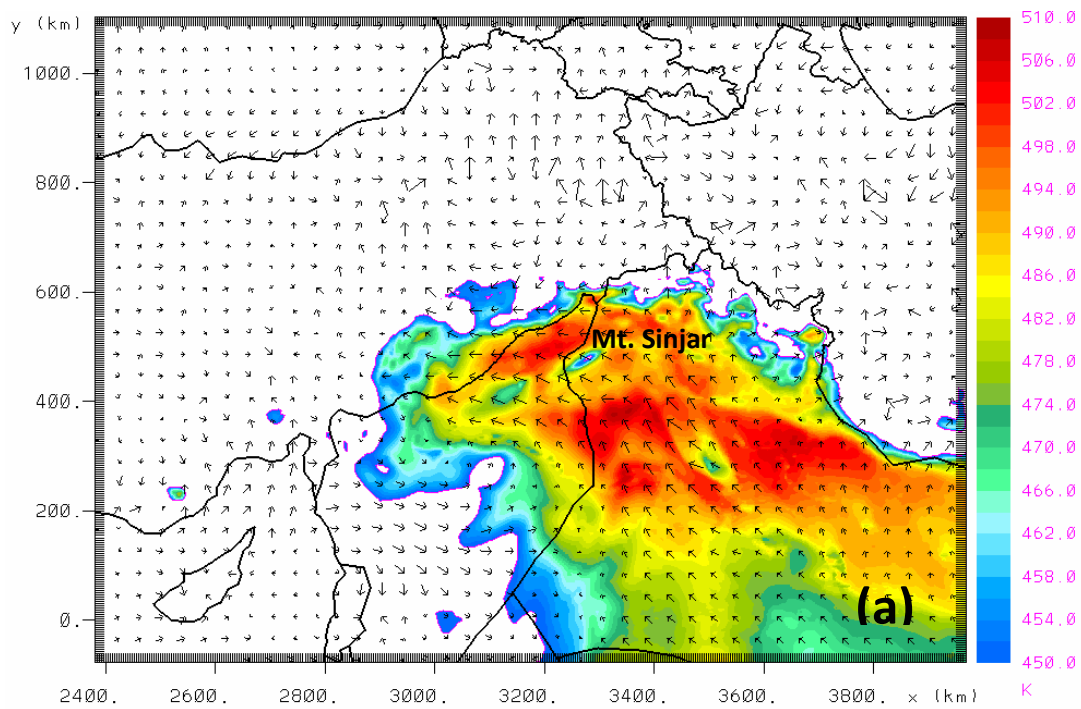


660  
661



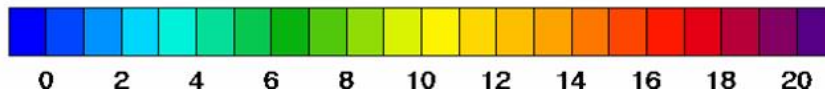
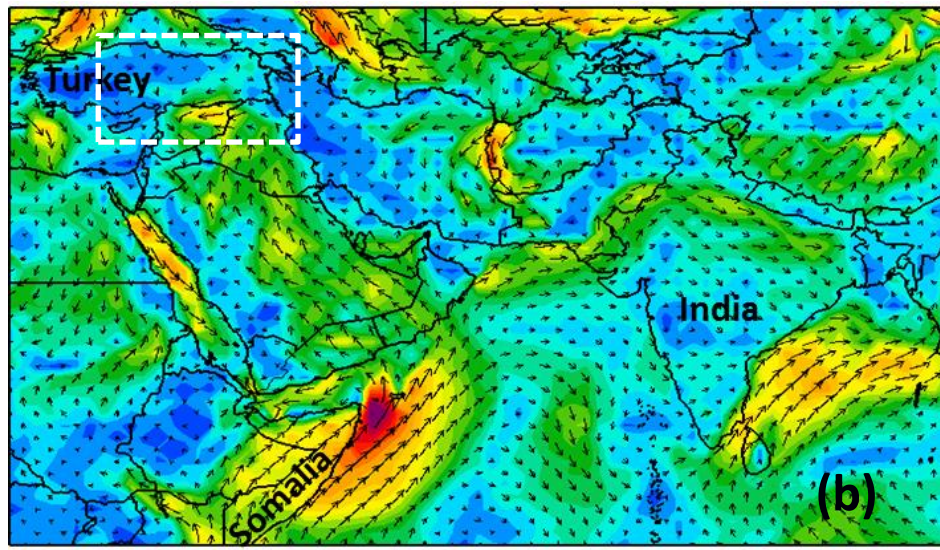
662  
663  
664  
665  
666  
667  
668  
669  
670  
671  
672

Figure 5. a) Model AOT at 550 nm (color scale) and cloud cover > 70% (red contour). b) MSG-SEVIRI dust RGB component, 7 September 2015, 00:00 UTC. The white rectangular approximately indicates the location of the model domain shown in Figure 5a.



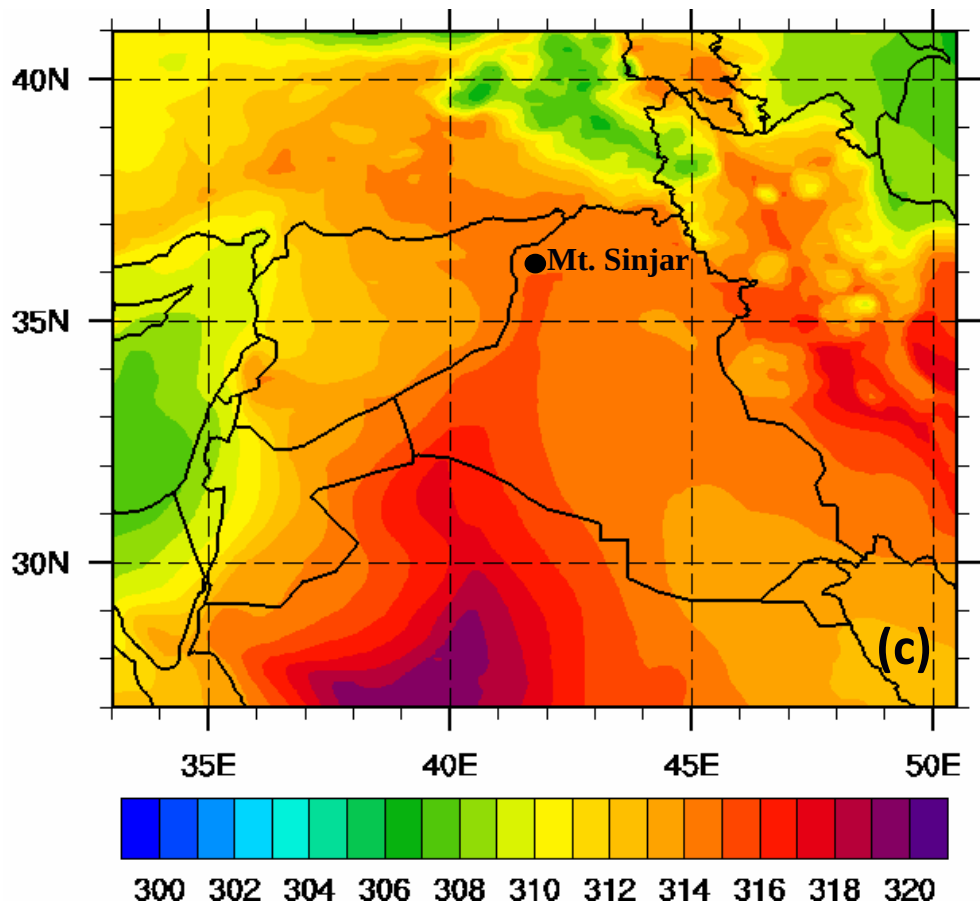
673

674



675

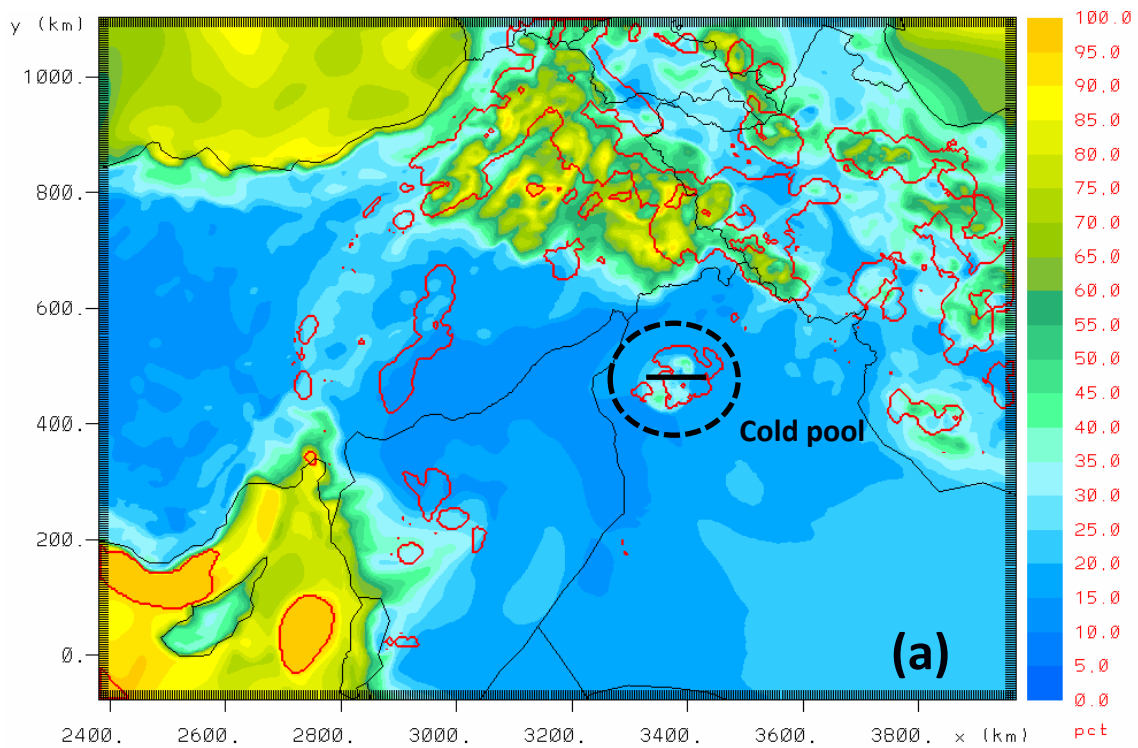
676 Figure 6. a) Model equivalent potential temperature (K) and wind vectors at 50m above ground, 6  
 677 September 2015, 13:00 UTC. b) Wind speed at 975 mb from the NCEP final analysis (FNL) dataset, 6  
 678 September 2015, 06:00 UTC. The white rectangular indicates the location of the model domain  
 679 shown in Figure 6a.



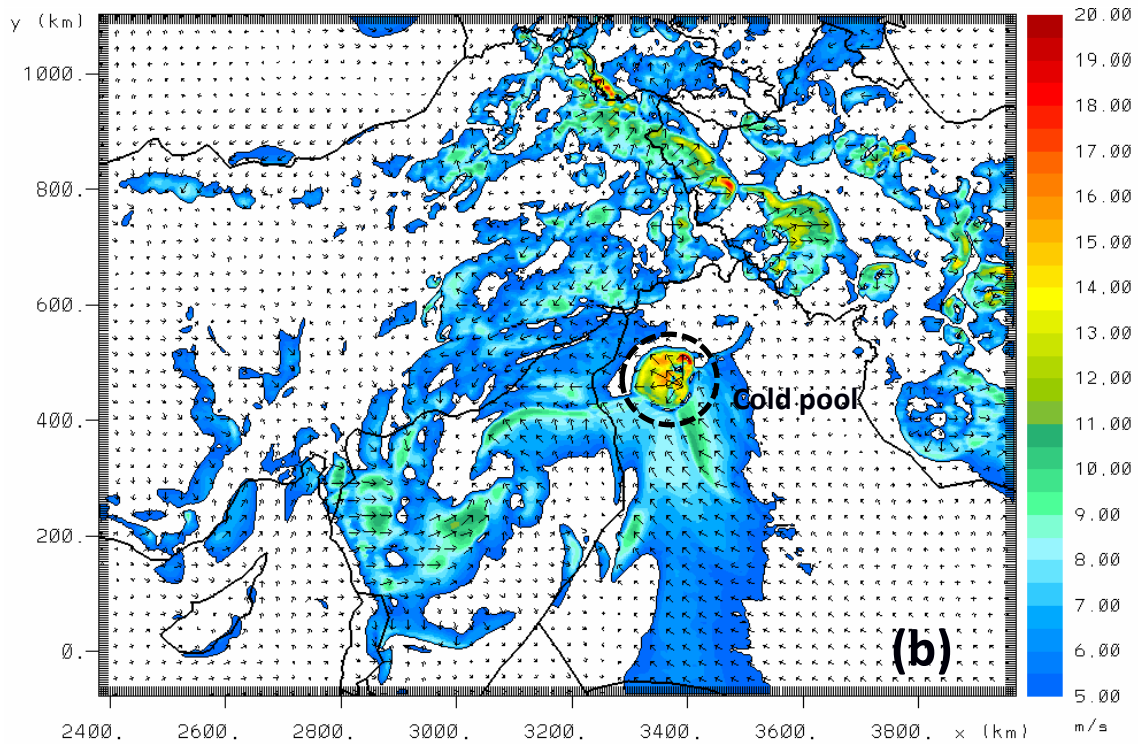
680  
 681 Figure 6. c) Model 1000-700 mb thickness (dam), 6 September 2015, 15:00 UTC

682  
 683  
 684  
 685



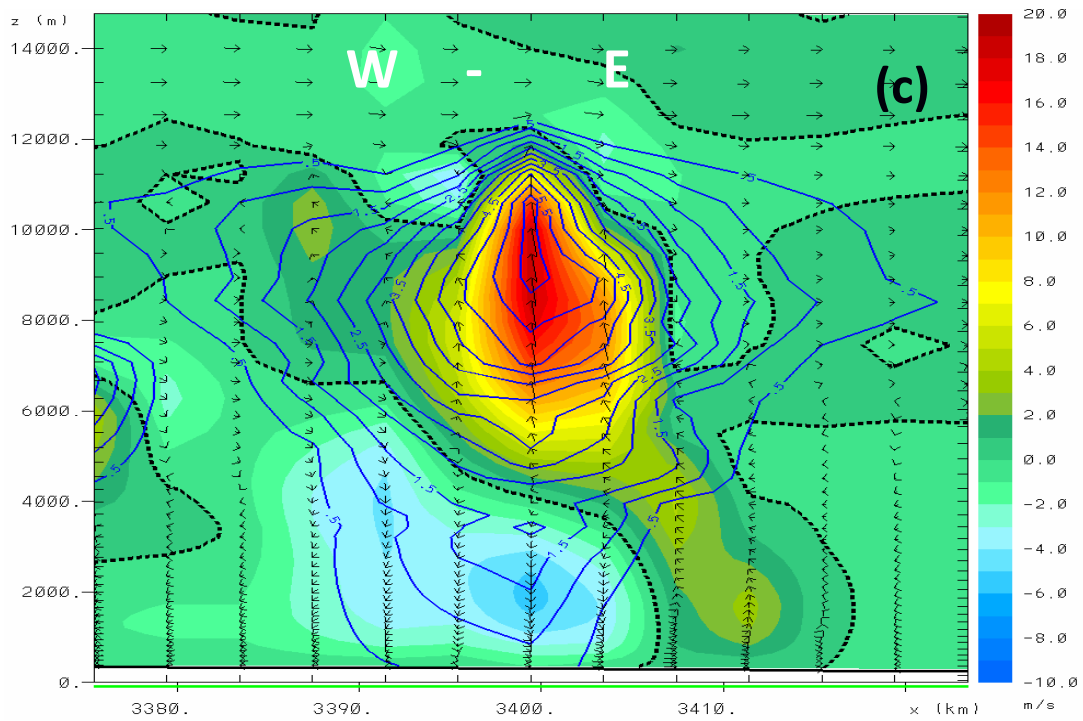


686

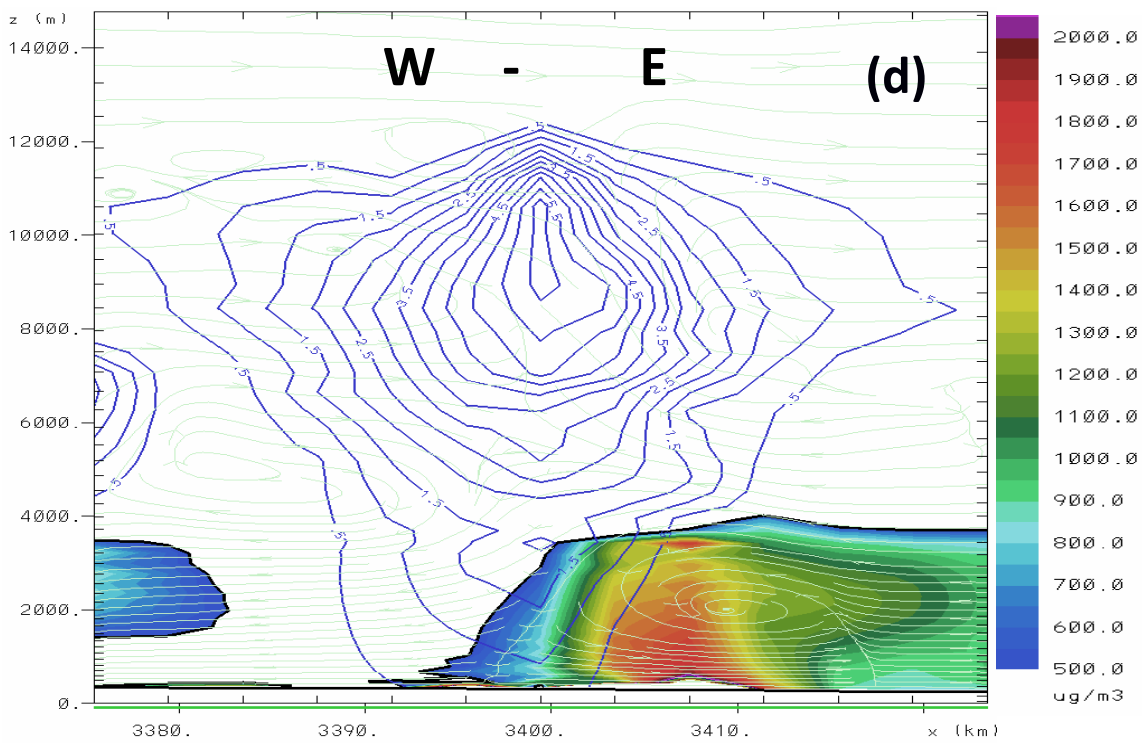


687

688 Figure 7. a) Model relative humidity at the first model level (color scale) and  $-20^{\circ}\text{C}$  iso-temperature  
 689 line (red contours) of rain droplets air temperature difference. b) Model wind speed at 10m ( $\text{ms}^{-1}$ ).  
 690 The dashed line denotes the location of the cold pool and the solid black line the location of the  
 691 storm cross-sections of Figures 7c,d.



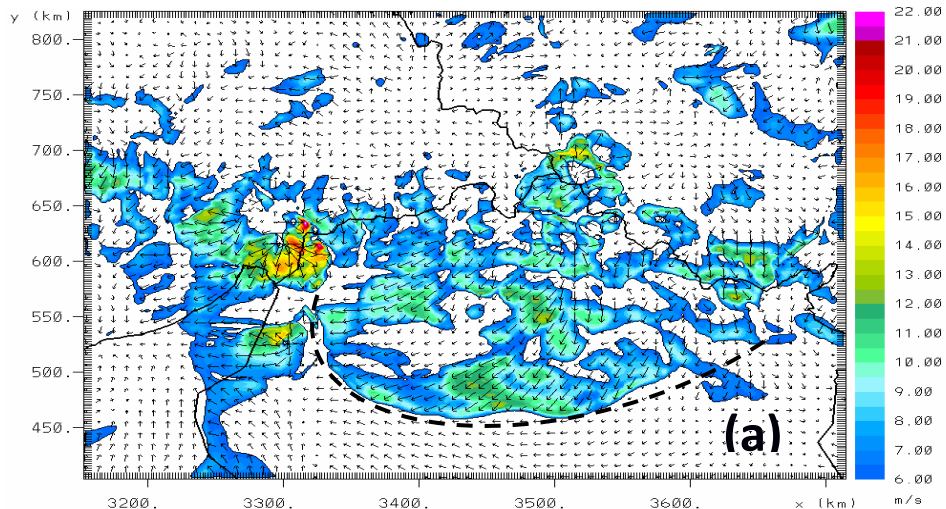
692



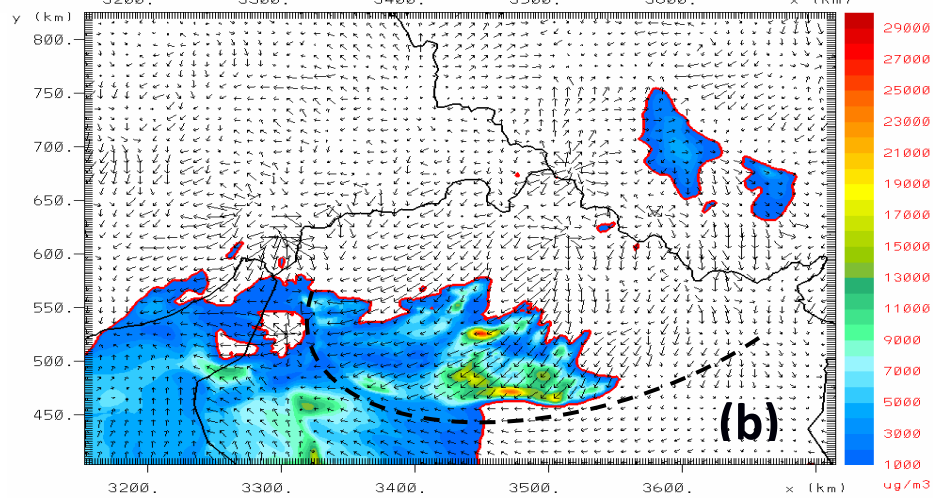
693

694 Figure 7. c) Vertical cross section of total condensate mixing ratio (blue contours in  $\text{g k g}^{-1}$ ) and  
 695 vertical wind component (vectors and color scale in  $\text{m s}^{-1}$ ). The dashed line separates updraft  
 696 (positive  $w$ ) from downdraft/precipitating regions (negative  $w$ ). d) Vertical cross section of total  
 697 condensate mixing ratio (blue contours in  $\text{g k g}^{-1}$ ), dust concentration ( $\mu\text{g m}^{-3}$ ) and flow streamlines,  
 698 6 September 2015, 15:00 UTC

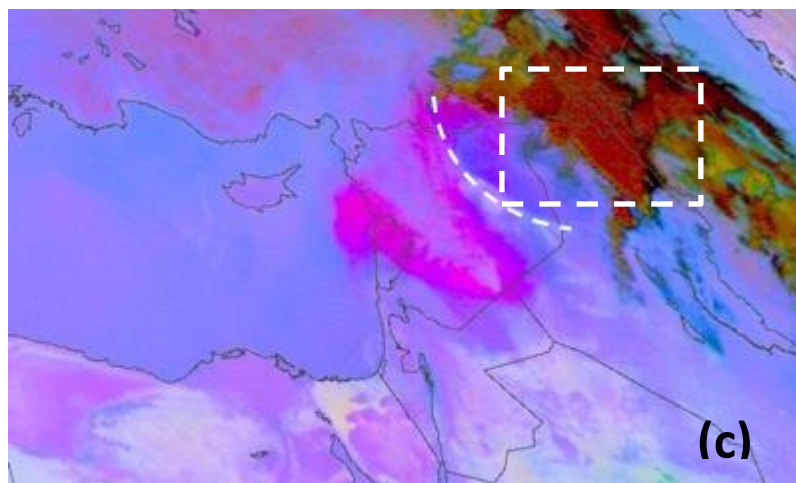
699



700



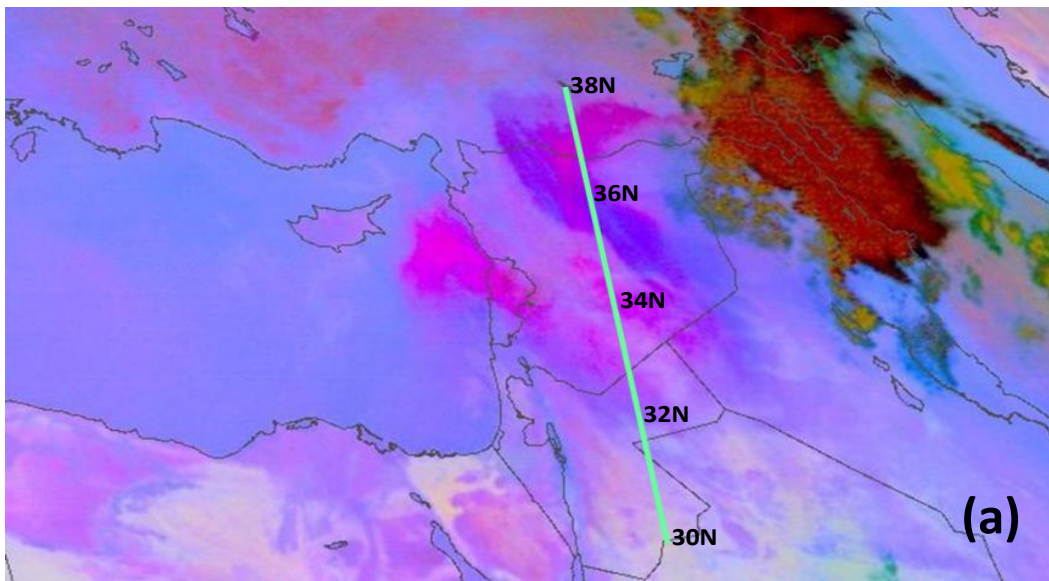
701



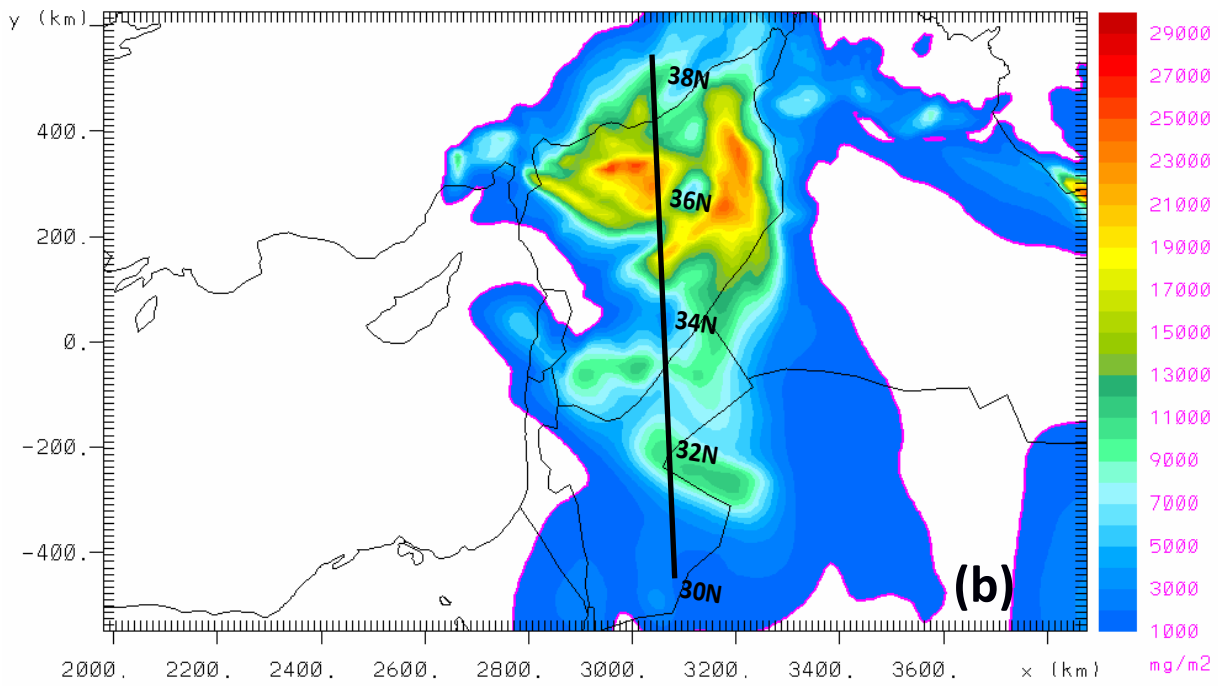
702

703 Figure 8. a) Model wind speed greater than  $6 \text{ ms}^{-1}$  at 10 m and b) Near surface model dust  
 704 concentration ( $\mu\text{g m}^{-3}$ ) from the inner grid ( $2 \times 2 \text{ km}$ ) c) MSG-SEVIRI RGB component, 6 September  
 705 2015, 20:00 UTC. The dashed lines indicate the haboob front location and the dashed rectangular in  
 706 Figure 8c approximately indicates the location of the model domains shown in Figures 8a,b.

707



708  
709

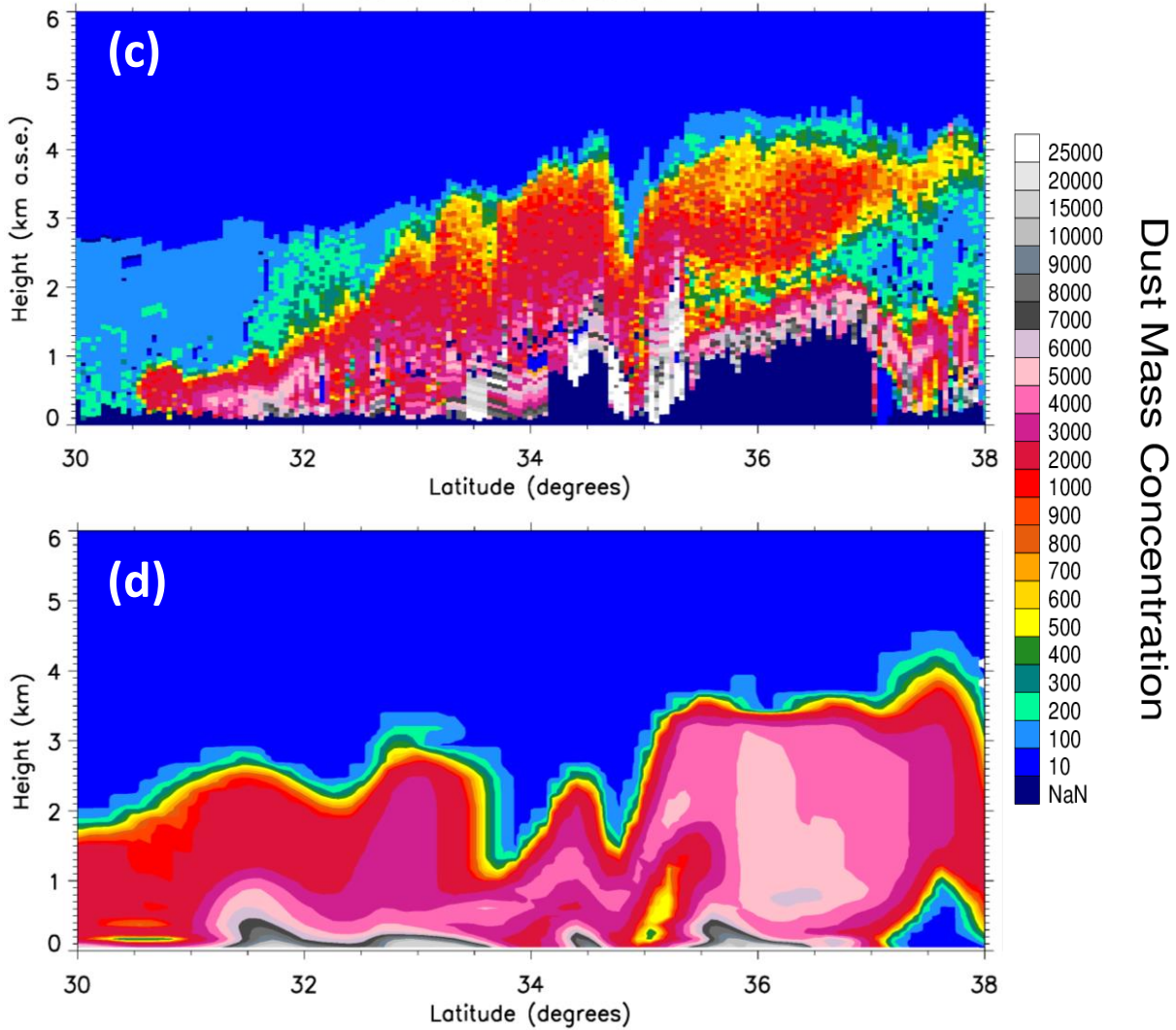


710

711 Figure 9. a) MSG-SEVIRI RGB map and CALIPSO overflight (green line) b) Model dustload ( $\text{mg m}^{-2}$ )



CALIPSO Dust Mass Concentration ( $\mu\text{g}/\text{m}^3$ )  
2015-09-06, 23:33 UTC



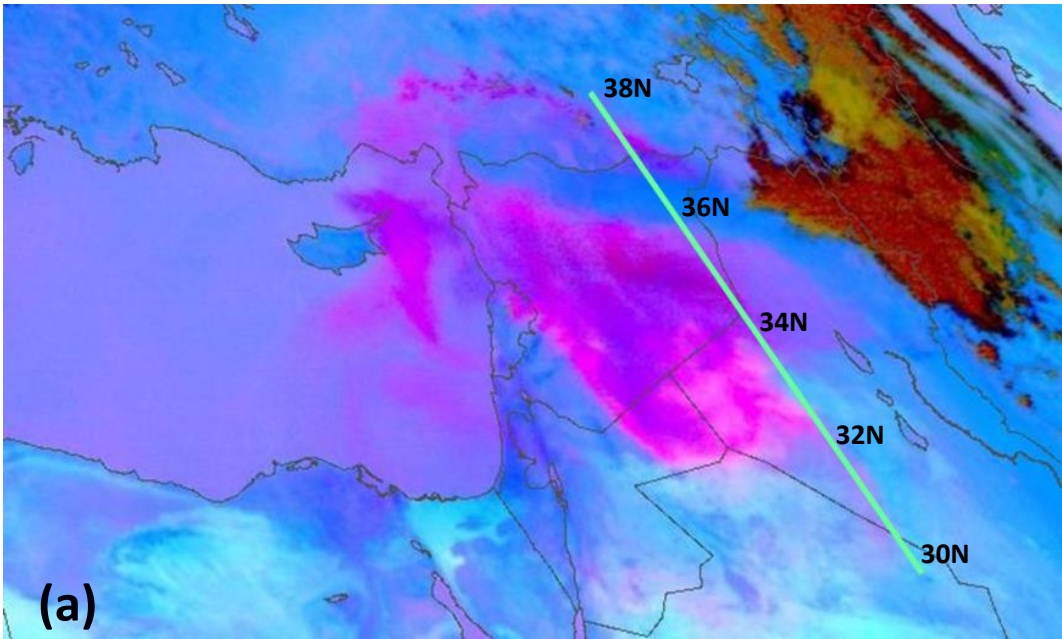
712

713

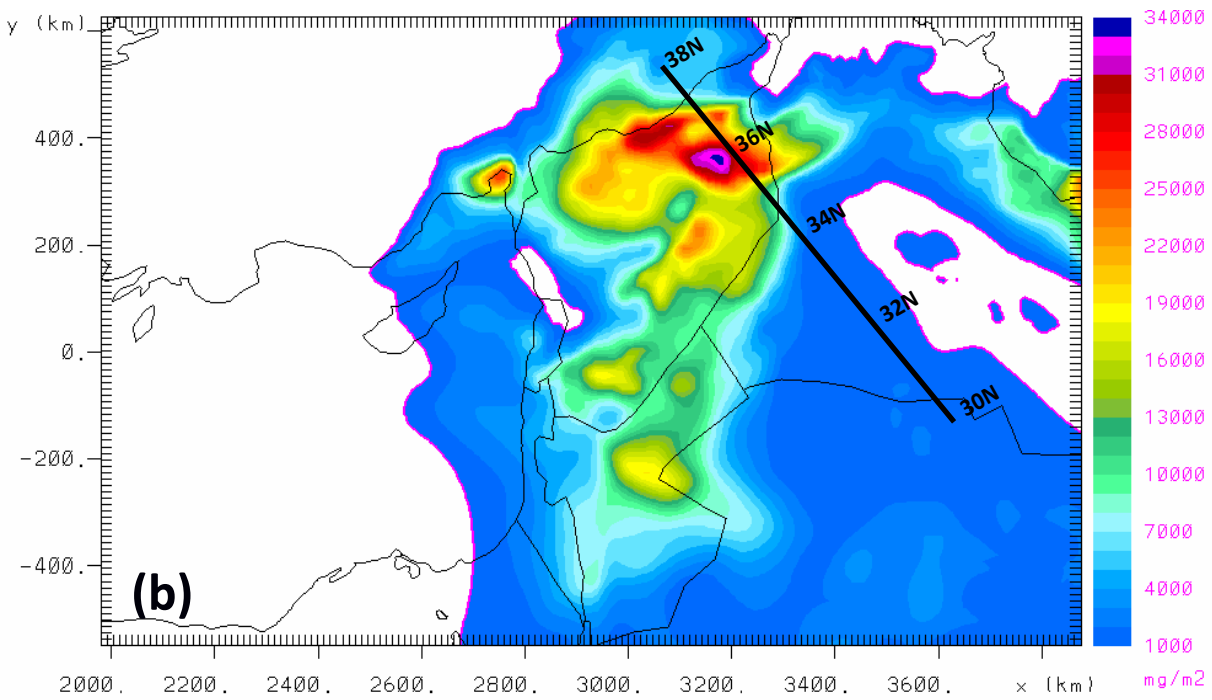
714 Figure 9. c) CALIPSO dust mass concentration ( $\mu\text{g m}^{-3}$ ) and d) model dust mass concentration at 6  
715 September 2015, 23:33 UTC. Due to the severity of the event CALIPSO signal is totally attenuated  
716 below  $\sim 1\text{km}$  a.s.e. in the area between  $35\text{-}37^\circ\text{N}$  (dark blue color).

717

718



719  
720  
721

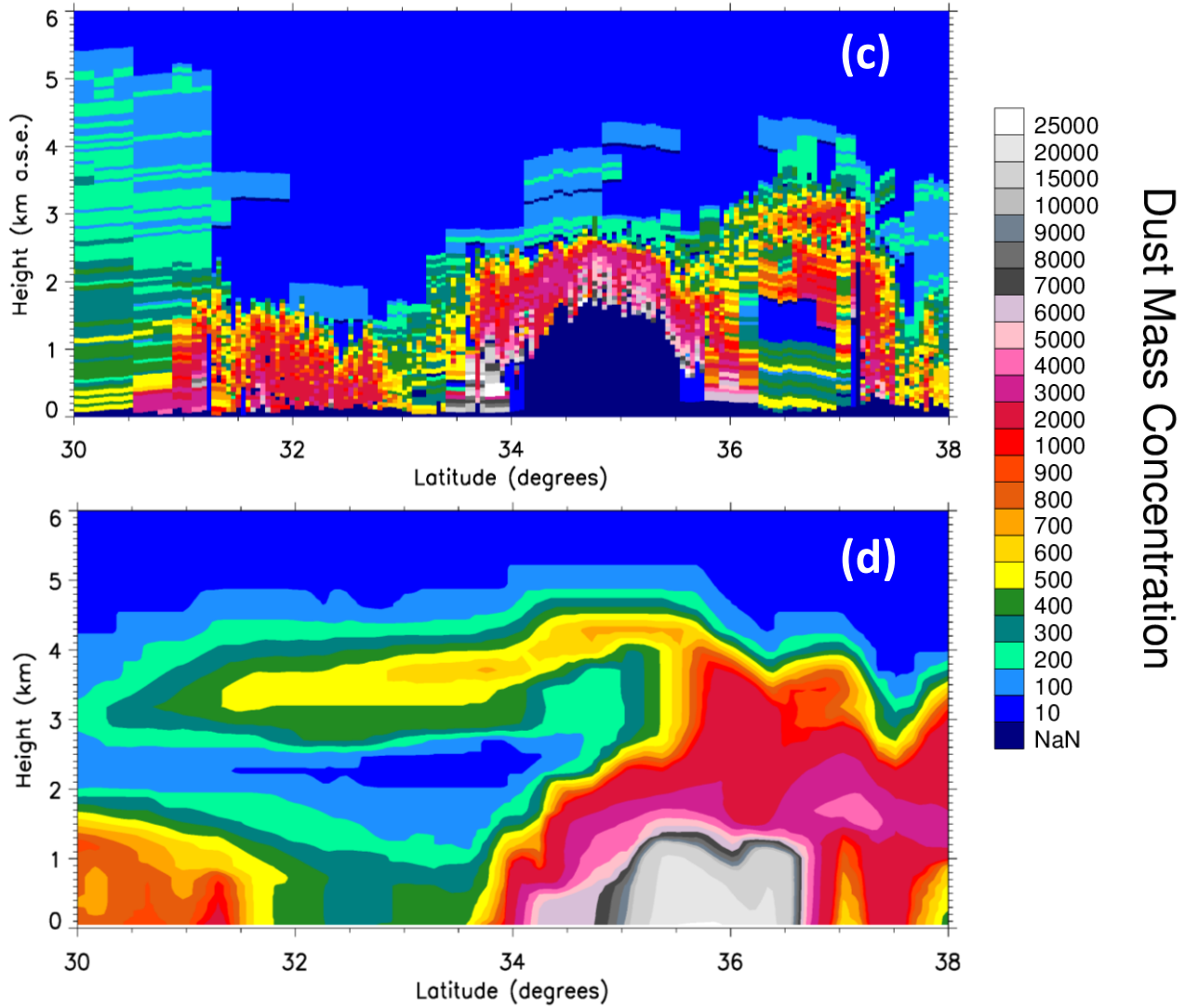


722  
723  
724

Figure 10. a) MSG-SEVIRI RGB map and CALIPSO overflight (green line), b) Model dustload ( $\text{mg m}^{-2}$ )

725

CALIPSO Dust Mass Concentration ( $\mu\text{g}/\text{m}^3$ )  
2015-09-07, 10:35 UTC



726

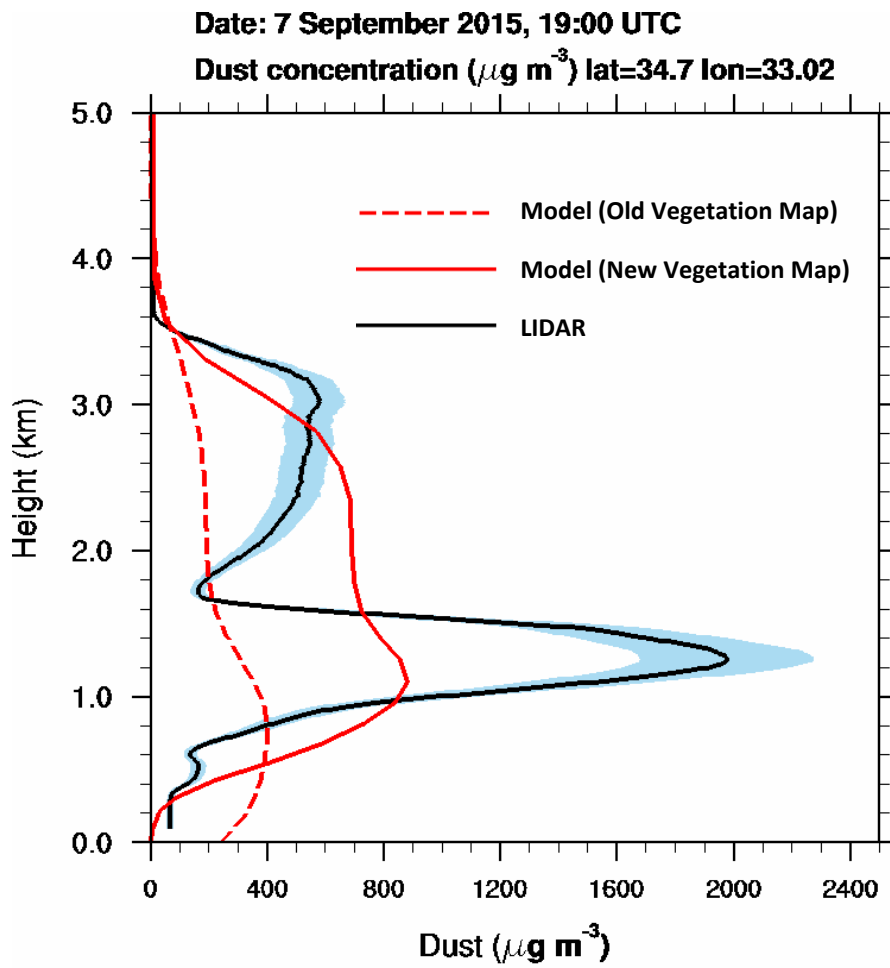
727

728 Figure 10. c) CALIPSO dust mass concentration ( $\mu\text{g m}^{-3}$ ) and d) model dust mass concentration at 7  
729 September 2015, 10:35 UTC. Due to the severity of the event CALIPSO signal is totally attenuated  
730 bellow  $\sim 1\text{km}$  a.s.e. in the area between  $34\text{-}36^\circ\text{N}$  (dark blue color).

731



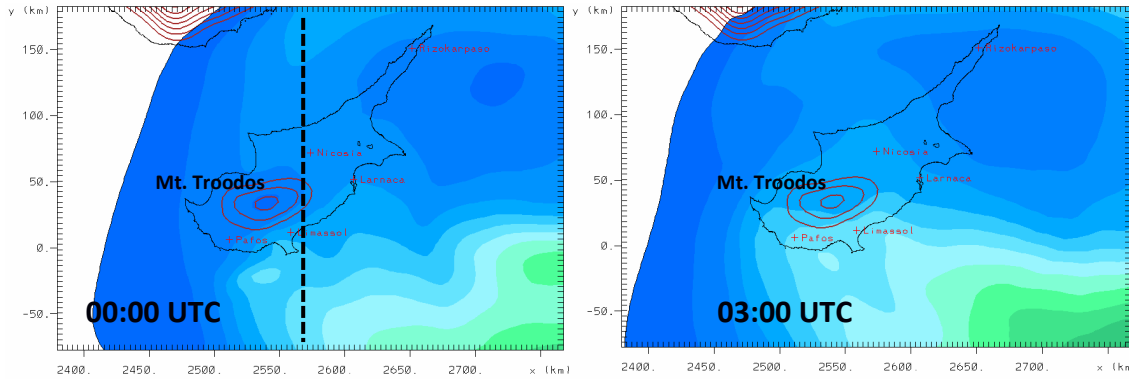
732  
733



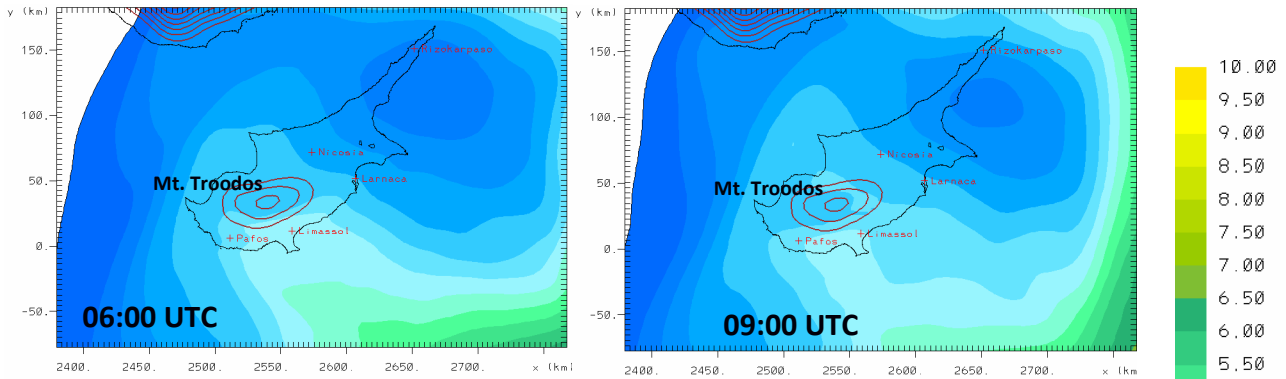
734  
735  
736

Figure 11. Vertical profile of dust concentration over Limassol on 7 September, 19:00 UTC. Blue shadow indicates a 20% uncertainty of the lidar measurements.

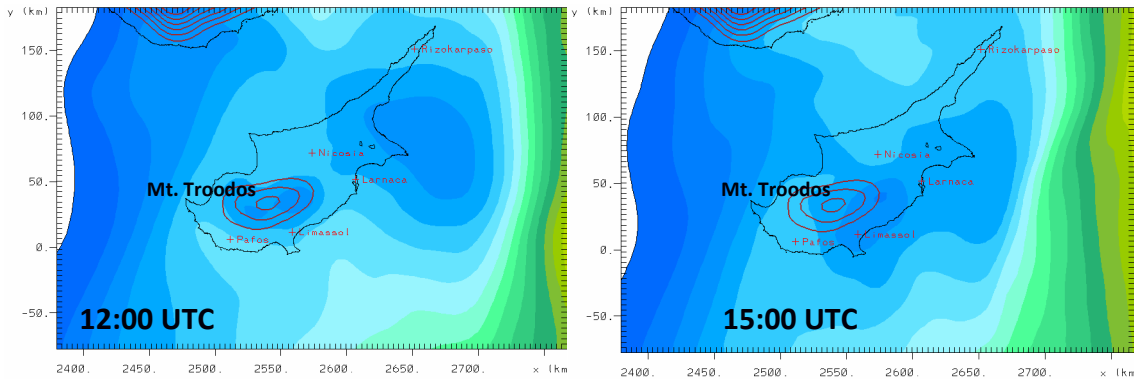
737



738



739

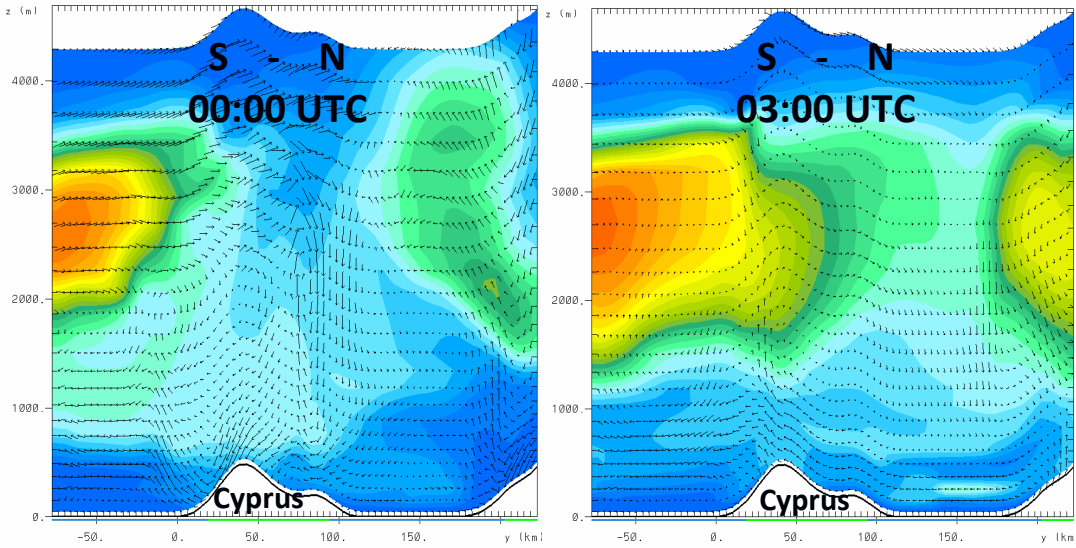


740

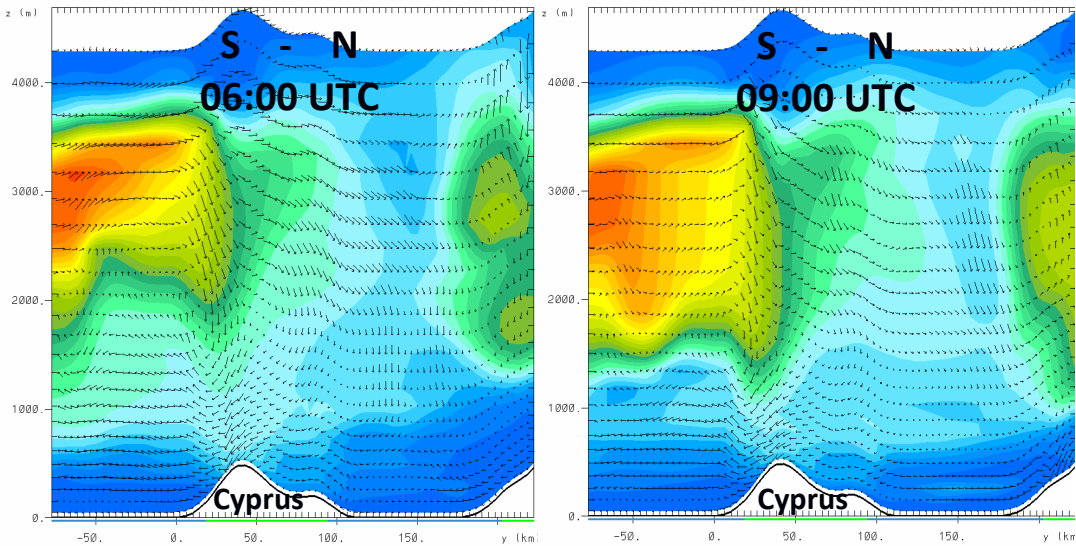
741 Figure12. Model 550 nm AOT over Cyprus 00:00 – 15:00 UTC, 8 September 2015, zoom from the  
 742 second (4x4 km) model domain. The dashed black line shows the location of the cross-sections in  
 743 Figure 13.

744

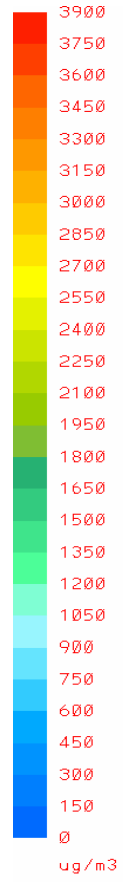
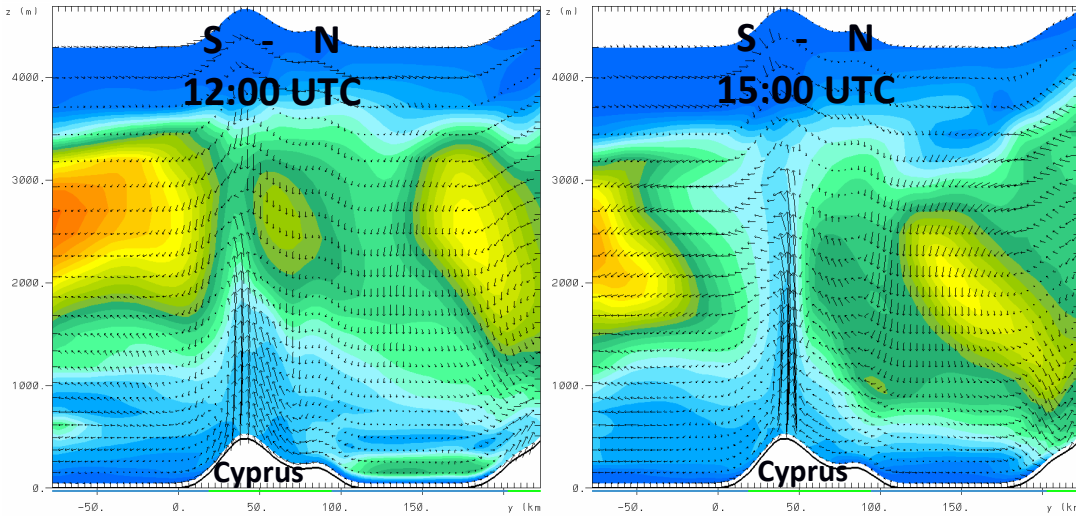
745



746



747



748 Figure 13. Vertical cross-section (South-North) of modeled dust concentration over Cyprus 00:00 –  
 749 15:00 UTC, 8 September 2015. The location of the cross-section is shown in Figure 12.

750